Weather Clim. Dynam., 7, 2327–2354, 2026
https://doi.org/10.5194/wcd-7-2327-2026
© Author(s) 2026. This work is distributed under
the Creative Commons Attribution 4.0 License.

Weather and Climate Dynamics
Open Access
EGU

Intermodel differences in seasonal and regional CMIP6 divergent atmospheric heat transport

Ruth Geen[1], **Robert Fajber**[2], **Marysa Laguë**[3], **and Ishani Mistry**[1]

[1]School of Geography, Earth and Environmental Science, University of Birmingham, Edgbaston, Birmingham, B15 2TT, United Kingdom
[2]Department of Atmospheric and Oceanic Sciences, McGill University, 845 Sherbrooke Street West, Montreal, QC, H3A 0G4, Canada
[3]Department of Geography, University of British Columbia, 1984 West Mall, Vancouver, BC, V67 1Z2, Canada

Correspondence: Ruth Geen (r.geen@bham.ac.uk)

Received: 12 May 2026 – Discussion started: 27 May 2026
Revised: 20 October 2026 – Accepted: 6 November 2026 – Published: 27 November 2026

Abstract. The tropical rainband's location is closely tied to divergent atmospheric heat transport (AHT). Recent work decomposed annual and zonal-mean AHT into radiative fluxes, evaporative fluxes and sensible heat, finding that the latitudinal structure of divergent AHT strongly resembled that associated with the evaporative fluxes, and that imposed changes to evaporation in model simulations altered total divergent AHT. Here, we generalise this decomposition to explore regional and seasonal intermodel differences in CMIP6 simulations.

In historical climate, we find that the spatial structure of the total JJA and DJF AHT most resembles that linked to evaporative and radiative fluxes. Intermodel differences in divergent AHT predominantly relate to east-west rather than north-south rainband shifts. In future climate, in JJA most models show enhanced southward interhemispheric energy transport, while in DJF models instead undergo a zonal change towards more energy export from a warmer eastern Pacific. We identify groups of models from different families that show similar decompositions of their total AHT response to climate change into the individual flux terms. This suggests that distinct storylines may exist through which warming affects the energy budget and associated tropical rainfall.

1 Introduction

The atmosphere-ocean system acts as a heat pump that transports moist static energy (MSE) poleward, driven by the gradient in net radiative input between the tropics and poles (Trenberth and Stepaniak, 2003, 2004). In the tropical atmosphere, this poleward atmospheric heat transport (AHT) is dominated by the upper branches of the Hadley circulation, due to strong advection of high geopotential upper-level air. The latitude at which the divergent vertically-integrated meridional AHT changes from negative (southward) to positive (northward) is described as the Energy Flux Equator (EFE) (Kang et al., 2008). The close relationship between upper-level mass transport and vertically-integrated divergent AHT means that the latitude of the EFE often provides a valuable proxy for the Intertropical Convergence Zone (ITCZ) latitude (Schneider et al., 2014). This study explores divergent AHT differences in present and future climate across models from Phase 6 of the Coupled Model Intercomparison Project (CMIP6).

The vertically-integrated divergent AHT can be analysed via the MSE budget, allowing shifts in the tropical rainband to be interpreted based on the top of atmosphere and surface energy fluxes. This energetic framework was originally developed in the annual and zonal mean, but has been shown to apply well on seasonal timescales (Adam et al., 2016a) and regionally (Adam et al., 2016b; Boos and Korty, 2016). Analysis of the MSE budget has proved useful in interpreting the response of the tropical rainband to a myriad of perturba-

tions, including anthropogenic global warming forcings and feedbacks (Mamalakis et al., 2021; Nicknish et al., 2023) and natural processes (Boos and Korty, 2016; Kang, 2020; Han et al., 2023).

Previous studies have also applied the energetic framework to the study of tropical rainfall biases within the CMIP models, for example the well-known double-ITCZ bias (Adam et al., 2016c, 2018; Kim et al., 2021; Ren and Zhou, 2024). Fewer studies have explored applications of the energetic framework to global monsoon biases and trends. A recent study (Chen et al., 2024) found that reduced biases in the Northern Hemisphere summer monsoon in CMIP6 compared to CMIP5 were associated with improvements in meridional AHT, with improvements in downward surface longwave radiative fluxes. Future changes to regional tropical rainfall have been found to relate to changes in energetic contrasts (Mamalakis et al., 2021; Nicknish et al., 2023), and observed trends in interhemispheric thermal contrast across CMIP6 models have been used as an emergent constraint on monsoon rainfall projections (Chen et al., 2022).

While the total energy flux of the combined ocean-atmosphere system is governed by TOA radiative fluxes (Trenberth and Stepaniak, 2003, 2004; Stone, 1978), the partitioning of the heat transport between the ocean and the atmosphere is controlled by the surface energy balance. At Earth's surface, the net downward shortwave is balanced by turbulent fluxes of latent and sensible heat, the net upward longwave, and surface heat uptake (more significant over the ocean). Since the AHT is in balance with the turbulent energy fluxes and the radiation absorbed by the atmosphere (difference between TOA and surface radiative fluxes), understanding the connection between the surface energy balance and AHT is essential in understanding the energetic constraints on AHT.

The interpretation of MSE budget changes can be influenced by the decomposition used. MSE comprises contributions from both dry static energy (DSE) and latent heat, and total AHT has commonly been examined in terms of these two components (Trenberth and Stepaniak, 2003; Yang et al., 2015; Donohoe et al., 2020). The DSE and latent heat budgets are interconnected via precipitation, which acts as a sink of latent heat when water vapor condenses, and a source of dry static energy due to the heat released during this condensation (Trenberth and Stepaniak, 2003).

A recent study by Fajber et al. (2023) decomposes AHT into components attributed to meridional gradients in fluxes of evaporation, sensible heat, and radiation. When this approach is applied, it can be seen that the spatial structure of the annual and zonal-mean meridional AHT strongly follows that implied by meridional gradients in evaporation, in both the mean state and in response to applied forcings. Fajber et al. (2023) argue that, compared with the DSE/latent heat decomposition, this decomposition captures the smooth handover of energy from moist to dry static energy via evaporation and condensation. They suggest that this indicates a central role for evaporation in the spatial patterns of AHT. As noted above, while the total heat transport of earth system is determined by the TOA radiation gradient, evaporation is the mechanism by which this gradient is mediated to the atmosphere. This is because the meridional structure of surface shortwave flux, temperature, and wind speeds (and, over land, soil moisture availability and transpiration), create a larger meridional gradient in the latent heat flux than the other terms in the atmospheric energy budget. This decomposition was applied in an assessment of the annual-mean model biases in partitioning of total meridional heat transport by the atmosphere and ocean across three CMIP phases (Donohoe et al., 2024). This revealed that excessive tropical evaporation appeared to enhance AHT at the expense of oceanic heat transport.

Here, we apply this AHT decomposition in tandem with the energetic framework for the tropical rainband to interpret the seasonal and long term shifts of the tropical rainbelts. Details of the EFE framework, the decomposition and the datasets used are provided in the "Methods" section. We assess the partitioning of the regional and seasonal patterns of divergent AHT, and the intermodel differences in AHT and tropical precipitation seen across CMIP6 in simulations of present and future climate. We first evaluate seasonal-mean horizontally divergent AHT, and its decomposition into turbulent and radiative fluxes, using CMIP6 model data and ERA5 reanalysis. We find that the seasonal and regional structure of total AHT strongly resembles that of the evaporation component. Next, we explore intermodel differences in AHT via analysis of cross-equatorial AHT and empirical orthogonal function analysis. Last, we analyse the principal components associated with the leading EOFs, and their breakdown into radiative, latent and sensible flux components. We use these to develop a framework for diagnosing pathways of bias and change across CMIP model families.

2 Methods

2.1 CMIP6 data

We use monthly data from three CMIP6 experiments. The *historical* simulation is a coupled-ocean experiment in which observed forcings are prescribed, including solar, volcanic, and anthropogenic forcings (Eyring et al., 2016). Monthly climatologies are constructed for the modeled period spanning 1980–2014. The *historical* simulation allows models to be evaluated against modern observations, but includes evolving greenhouse gas concentrations, and so a climate change signal. We therefore also use data from the *piControl* simulation, in which CO_2 concentrations are prescribed at preindustrial levels, to confirm that the features identified in the *historical* dataset are not a consequence of forced trends in the data. 400 years of data were used to create a climatology for each model, except for CNRM-CM6-1-HR,

for which only 300 years were available. Further details on the periods used can be found in Appendix A. To examine forced responses to climate change, we compare the *SSP5-8.5* simulation (O'Neill et al., 2016) to the *historical* simulation. This simulation is selected to provide a strong end-of-century forcing such that the forced signal emerges from internal variability.

Models were selected based on availability of monthly-mean data for 18 variables: surface pressure (ps), near surface air temperature (tas), surface temperature (ts), latent heat flux (hfls), sensible heat flux (hfss), shortwave and longwave top of atmosphere and surface radiative fluxes (rsdt, rsut, rsds, rsus, rlut, rlds, rlus), precipitation (pr), air temperature (ta), specific humidity (hus), geopotential height (zg), zonal and meridional windspeed (ua, va). Data from 40 models (24 model families) are used for the *historical* and *piControl* simulations and 35 models for the *SSP5-8.5* simulation. One variant is used per model, with the same variant used across simulations where possible. Table A1 lists the models and variants used. Data from all models were re-gridded to a 2.5° grid.

Humidity and dry static energy transports are not available for the majority of CMIP6 models. Windspeed, temperature, humidity and geopotential data are provided having been interpolated to default pressure levels, with the best data availability at daily or monthly timescales. This makes it difficult to accurately evaluate vertically integrated MSE fluxes directly from u, v, and h. The divergent AHT and χ were instead inferred from the net flux of energy into the column and the column energy tendency, $\partial_t\langle e\rangle$, using Eq. (6).

2.2 ERA5 reanalysis data

ERA5 is ECMWF's fifth generation reanalysis product, combining model data and observations to produce a best estimate of the state of the atmosphere, land surface and ocean (Hersbach et al., 2023). We use this dataset as a point of comparison for the CMIP6 models with observed climate. However, in contrast to CMIP6 models, the ERA5 atmospheric energy budget is not closed (Donohoe et al., 2024; Mayer et al., 2021a). We find that evaluating the MSE fluxes following Eqs. (6) and (7) gives a spurious EFE, which sits much further poleward than expected, e.g. over southern Italy and northern California in July. We therefore instead use the mass-consistent total energy fluxes to estimate the total divergent MSE flux (Mayer et al., 2021b). This includes a contribution due to kinetic energy. Comparison of the magnitude of the total energy flux to the non mass-consistent vertical integral of kinetic energy transport confirms this term is negligible compared to the MSE contributions. Partitioning by latent heat, sensible heat, radiation and storage is then estimated from the relevant fluxes and the column integrated tendency.

Due to the above limitations, a direct model-to-reanalysis comparison is not possible. The study therefore primarily focuses on intermodel differences, rather than model biases, with climatologies of monthly-mean data for 1980–2014 from ERA5 used as a sense-check of the model behavior.

2.3 Energy budget decomposition

The vertically integrated MSE budget can be written:

$$\partial_t\langle e\rangle + \nabla\cdot\langle \boldsymbol{u}h\rangle = F_{\mathrm{NET}}, \tag{1}$$

where angular brackets indicate a vertical integral and $\boldsymbol{u}$ is the horizontal wind vector. h is MSE, the sum of potential energy and moist enthalpy, and e is the sum of internal, latent and potential energy:

$$h = c_pT + L_{\mathrm{v}}q + gz \tag{2}$$

$$e = c_vT + L_{\mathrm{v}}q + gz. \tag{3}$$

In the above, c_p is the heat capacity of air at constant pressure, c_v is the heat capacity of air at constant volume, T is temperature, L_{v} is the latent heat of vaporisation of water, q is specific humidity, g is gravitational acceleration, and z is geopotential height. F_{NET} describes the net flux of energy into a column of air due to radiative (RAD) and turbulent (latent, LH, and sensible, SH) heat fluxes:

$$F_{\mathrm{NET}} = \mathrm{LH} + \mathrm{SH} + \mathrm{RAD} \tag{4}$$

The net radiative flux into the column is comprised of the top of atmosphere, TOA, and surface, SURF, shortwave, SW, and longwave, LW, fluxes:

$$\begin{aligned}\mathrm{RAD} = {}& \mathrm{SW}_{\mathrm{TOA}\downarrow} - \mathrm{SW}_{\mathrm{TOA}\uparrow} - \mathrm{LW}_{\mathrm{TOA}\uparrow} \\ & + \mathrm{SW}_{\mathrm{SURF}\uparrow} - \mathrm{SW}_{\mathrm{SURF}\downarrow} + \mathrm{LW}_{\mathrm{SURF}\uparrow} \\ & - \mathrm{LW}_{\mathrm{SURF}\downarrow}.\end{aligned} \tag{5}$$

Equation (1) can be expressed in terms of an Energy Flux Potential, χ (Adam et al., 2016b) as

$$\nabla^2\chi = F_{\mathrm{NET}} - \partial_t\langle e\rangle. \tag{6}$$

Solving the above for χ, using the the Python package `Pyspharm`, allows the divergent components of the vertically integrated MSE flux to be evaluated locally as

$$(\partial_x\chi, \partial_y\chi) = (uh, vh). \tag{7}$$

The meridional minimum in χ corresponds to the EFE. Zonal minima have been defined as Energy Flux Prime Meridians (EFPMs) (Boos and Korty, 2016). We partition χ into components due to fluxes of radiation, latent heat, and sensible heat. To do this, we remove a global mean from each term to isolate the spatial gradients which are responsible for driving heat transport, and then solve Eq. (6). To close the budget within seasonal climatologies, an additional term, χ_{STOR}, describing atmospheric storage, $-\partial_t\langle e\rangle$, is included:

$$\chi = \chi_{\mathrm{RAD}} + \chi_{\mathrm{LH}} + \chi_{\mathrm{SH}} + \chi_{\mathrm{STOR}}. \tag{8}$$

Using the above, uh and vh are similarly partitioned into terms associated with these components.

2.4 Quantification of rainband latitude

In Sect. 3.3, we look at intermodel correlations between AHT at the equator, and the rainband latitude. The rainband latitude is quantified via the precipitation centroid (Frierson and Hwang, 2012), and the latitude of maximum precipitation. To evaluate the former, precipitation between -20 and 20° N is first weighted by the cell area, then zonally integrated and interpolated to 0.1°. The centroid is then the latitude for which there is equal area-weighted precipitation to the north and south. For the latitude of maximum precipitation, a zonal mean is taken, and the data is again interpolated to 0.1°, and the latitude of the maximum identified. A comparison of the precipitation centroid and maximum precipitation latitude for each model and season is shown in Fig. B1.

2.5 Intermodel EOF analysis

In Sect. 3.3, we examine the leading order intermodel Empirical Orthogonal Functions (EOFs) of χ. These are evaluated using the Python package eofs (Dawson, 2016). For each season, data from all 40 models is loaded and the multi-model mean evaluated and subtracted. Data is weighted by $\sqrt{(\cos\phi)}$, and Principal Component Analysis is performed across models to identity the leading modes explaining intermodel variance.

In Sect. 3.4, we evaluate pseudo-PCs in this PC space for ERA5's and *SSP5-8.5*'s χs, and for the *historical* and *SSP5-8.5* breakdown into χ_{RAD}, χ_{LH}, χ_{SH}, and χ_{STOR}. In all cases, we first remove the *historical* multi-model mean of χ, and then use eofs' "projectField" method to project the new field onto the existing solver for the intermodel *historical* χ EOF.

When visualizing the projected components, for the *historical* simulation, $(0, 0)$ indicates the multi-model mean of *historical* χ. However, when looking at the breakdown of shifts under *SSP5-8.5* in Fig. 11, and when performing hierarchical clustering over these changes, each model's *historical* PCs of χ are removed from the *SSP5-8.5* pseudo-PCs of χ and its breakdown, so that for all models $(0, 0)$ represents that individual model's *historical* χ PC.

3 Results

Throughout the paper, energy fluxes are partitioned into components associated with radiative fluxes, latent and sensible heat, and storage, using Eq. (8). We first examine this partitioning on seasonal and regional scales. We then use this approach to diagnose intermodel differences in historical climate and future trends. This provides insight into how the TOA radiation gradient is transmitted to the atmosphere in different models via surface heat exchange, although we note that the causes of differences and trends cannot be directly inferred in this way.

3.1 Zonal mean transports

Figure 1 shows zonal-mean fluxes contributing to the net energetic input (NEI) into the atmosphere (left) and the AHT attributed to each term (right). Consistent with previous work (Fajber et al., 2023), in the annual mean (Fig. 1a), the CMIP6 multi-model mean atmospheric energy inputs from sensible heat and radiation are relatively flat. The structure of the total net column energy input strongly resembles the latent heat flux. Accordingly, annual-mean AHT attributed to sensible heat and radiation is small, with the meridional structure of AHT strongly resembling that attributed to the latent heat flux (black and green lines, Fig. 1b). Compensation between AHT components attributed to latent heat, sensible heat and radiative fluxes leads to a near-zero AHT at the equator. AHT components from ERA5 are shown as dashed lines in the right column. Overall, the structure and magnitude of AHT in the CMIP6 multi-model mean closely follows that of ERA5.

On seasonal timescales, the overall structure of AHT continues to mirror that of the latent heat-attributed AHT, but other terms now become larger in magnitude. As expected from the seasonal cycle of insolation, radiative fluxes show interhemispheric contrast between seasons, with the Spring/-Summer hemisphere receiving greater net radiative input (orange lines, left-hand panels). This is reflected by a significant cross-equatorial AHT attributed to net radiative input throughout the year (orange lines, right-hand panels), which peaks over the equator in the solstitial seasons, and in the subtropics in the shoulder seasons. Although the structure of total AHT most strongly resembles that of the latent heat attributed component, in the solstitial seasons the sign of AHT at the equator follows that of the radiative input component. This is consistent with a cross-equatorial Hadley circulation that transports energy from summer to winter hemisphere in its upper branch, and moisture from winter to summer hemisphere in the lower branch. Throughout the year, the sensible heat flux, and the AHT attributed to this remains small (red lines).

When partitioning the energy fluxes within individual seasons, the tendency of column energy does not average to zero, as is the case for the annual-mean, as there is local warming and cooling at different times throughout the year. The pink lines in Fig. 1 illustrate the "storage" AHT term obtained when this tendency is used in solving Eq. (6). This term is strongest in the shoulder seasons, when the summer hemisphere is warming and winter hemisphere is cooling. It takes a sign implying a net horizontal transport of energy into the warming hemisphere, which approximately balances the AHT attributed to radiative fluxes in the shoulder seasons, and is small when averaged in the solstitial seasons. This term could thus be interpreted to diagnose local atmospheric warming and cooling arising from radiative processes, which is strongest in the shoulder seasons.

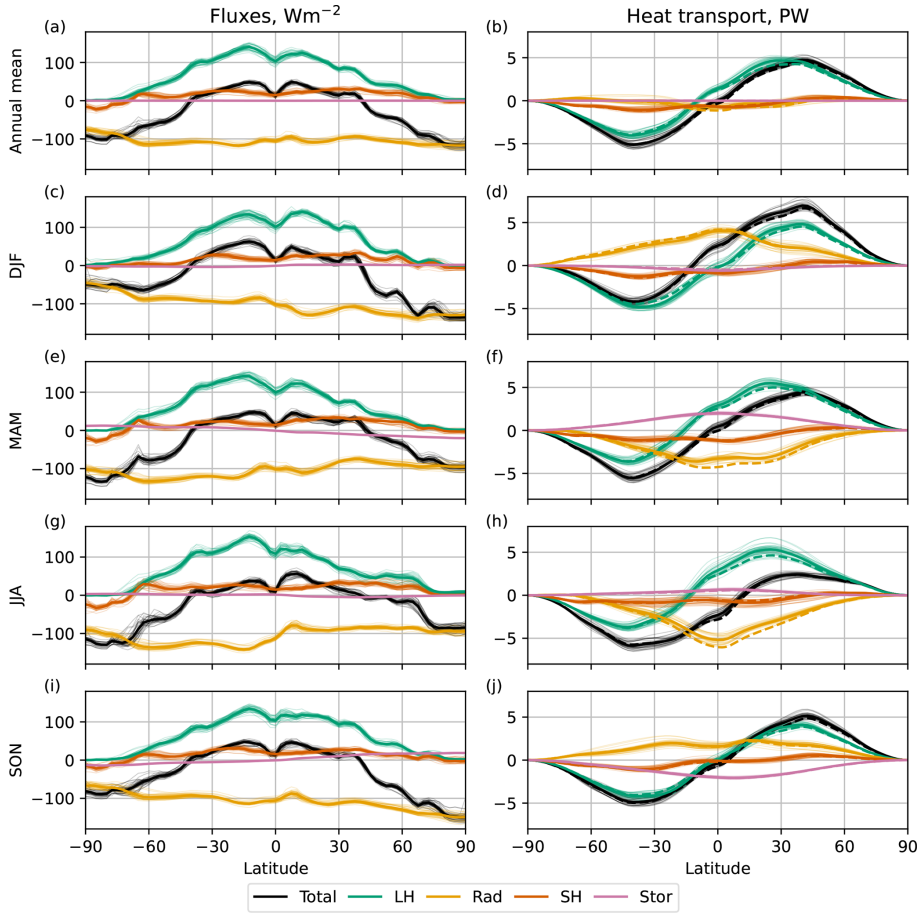

Figure 1. Climatological-mean fluxes (left column) and zonally-integrated implied heat transport (right column) for (top to bottom): the annual mean, DJF, MAM, JJA and SON. Thick, solid lines show the multi-model mean, dashed heat transport lines shown the estimate from ERA5. Thin lines indicate results for individual models. Colours represent net column flux/total AHT (black), and fluxes/AHT attributed to net column radiative input (orange), latent heat (green) sensible heat (red) and storage (pink). Pink lines show $-\frac{\partial e}{\partial t}$ (left column), and the "storage" AHT associated with this (right column).

3.2 Spatial structure

Figure 2 shows the multi-model mean χ in JJA (Fig. 2a) and DJF (Fig. 2b). Divergent heat transport is directed away from minima of χ, converging towards the maxima (see Eq. 7). By definition, the EFE follows the latitudinal minimum of χ, and EFPMs can be identified along the longitudinal minima (Boos and Korty, 2016); these are indicated by the magenta lines for each season in Fig. 2a and b. The multi-model mean χ (shading) resembles that identified in previous studies (Boos and Korty, 2016), and closely follows that evaluated from ERA5 (black contours) in both magnitude and structure. In JJA, a clear Northern Hemisphere minimum is seen over Eurasia, centered on South Asia. This indicates MSE divergence from this region and convergence at higher latitudes, particularly over Antarctica and the Southern Ocean. In DJF, this minimum and the associated EFPM shift eastward over the Western North Pacific (cf. seasonal monsoon mode shifts of Tuckman et al., 2024), with a secondary minimum over South America, and strongest MSE convergence over the Arctic and Northern Hemisphere land.

The remaining panels show χ components attributed to radiation, latent heat, sensible heat and storage. It can be seen that the radiative and latent heat components dominate the overall structure of χ. The associated energy fluxes can be seen in Fig. B2 (Appendix B), alongside a breakdown of the radiative terms in Figs. B3–B6. In both JJA and DJF, the latent heat contribution links to export of energy from the tropics towards the poles and, broadly speaking, from ocean towards land. This is intuitive, in terms of moist enthalpy entering the atmosphere via evaporation over waters warmed by insolation. The radiative contribution links to export of energy from the summer to the winter hemisphere (shortwave), and from arid land regions towards ocean (longwave).

In DJF, the zonal structure is dominated by the latent heat component (Fig. 2f), which has a strong minimum over the Pacific ocean due to strong evaporation over low-latitude ocean. The radiation attributed component (Fig. 2d) con-

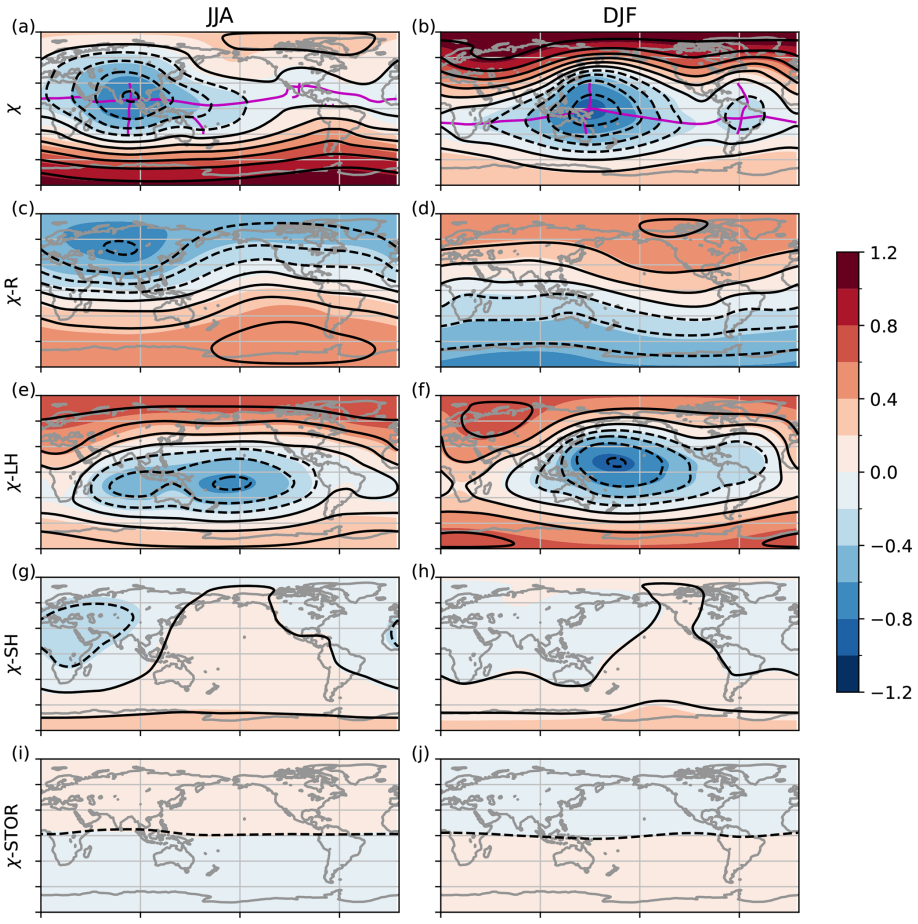

Figure 2. Climatological-mean Energy Flux Potential (χ, PW) for the CMIP6 multi-model mean (colors) and ERA5 (black contours) associated with (top to bottom): total energy flux divergence, χ, column radiative heating, χ-R, latent heat flux, χ-LH, sensible heat flux, χ-SH, column heat storage, χ-STOR. Left column shows JJA, right column shows DJF. Magenta lines show the EFE and EFPMs. EFPM lines are shown between 30° N and S, following Boos and Korty (2016).

tributes to interhemispheric contrast, via shortwave warming of the southern hemisphere (Fig. B5j). It also supports a slight westward shift in the total χ minimum relative to that of the latent heat component. We find that this is linked to a weaker surface longwave flux over the Pacific vs the land masses and Atlantic (Figs. B5i and B6i). In JJA, the structure of the latent heat component is broadly similar to that in DJF (Fig. 2e), with a minimum spanning the Indian Ocean and Pacific. In this season, the radiation-attributed component of χ (Fig. 2c) shows a regional minimum over Eurasia, linked to land-sea contrast in the net longwave surface flux (Figs. B3 and B4). This arises from weaker downward longwave surface fluxes over land where humidity is lower (Fig. B3e), particularly more arid regions, combined with stronger upward longwave surface fluxes over land (Fig. B3g), due to warmer surface temperatures relative to ocean. This radiation component of χ supports a more pronounced westward shift of the overall minimum in χ relative to that of the latent heat component than is seen in DJF.

The latent heat component (Fig. 2e and f) maximizes over the tropical oceans in both seasons, in particular over the Pacific Ocean, east of the maximum in χ. In the zonal-mean (Fig. 1d and h), the zonally varying pattern of χ-R cancels and the meridional structure of AHT resembles that of the latent heat component, cf. Fajber et al. (2023). However, Fig. 2 highlights that the longitudinal structure is also strongly influenced by the radiative contribution over land, particularly in JJA. Sensible heat (Fig. 1g and h) and storage terms (Fig. 1i and j) are relatively weak in both DJF and JJA. In both seasons, the sensible heat component of χ shows positive values over the Pacific and Southern Ocean, and negative values over most of global land, reflecting the stronger sensible heat flux over land regions relative to ocean. The storage term indicates convergence into the summer hemisphere, as would be expected from seasonal warming.

Mechanistically, Fig. 2 supports that the equator-to-pole gradient in the net TOA radiative flux drives poleward heat transport in the atmosphere by generating stronger tropical vs

Table 1. Intermodel standard deviations of total AHT_{eq} and that attributed to each component for the annual mean and each season (PW).

	Ann	DJF	JJA	SON	MAM
AHT_{eq}	0.17	0.35	0.33	0.28	0.24
AHT_{eq}-R	0.19	0.29	0.41	0.27	0.24
AHT_{eq}-LH	0.22	0.42	0.52	0.26	0.24
AHT_{eq}-SH	0.14	0.17	0.31	0.15	0.17
AHT_{eq}-STOR	0.003	0.08	0.08	0.11	0.09
AHT_{eq}-TURB	0.18	0.38	0.42	0.24	0.20

high latitude fluxes of moisture into the atmosphere. This energy input can be expected to drive tropical convection, and poleward MSE transport in the Hadley circulation at low latitudes. Shortwave radiation directly warms the summer hemisphere air relative to the winter hemisphere, driving cross-equatorial energy transport. Zonally, more energy is supplied to the atmosphere by evaporation over ocean than land. However, land-ocean contrasts in temperature and humidity, and the associated surface longwave fluxes, tend to completely (JJA) or partially (DJF) counteract this, enhancing heat input into the atmosphere over continents compared with oceans, particularly the Pacific.

3.3 Intermodel differences

3.3.1 Cross-equatorial AHT

From Fig. 1, it can be seen that individual models (thin lines) reproduce the broad-scale structure seen in ERA5. Intermodel differences are small compared to the overall magnitudes of the fluxes and heat transport, but are apparent throughout the year, particularly in the solstitial season. In the annual mean, differences throughout the year appear to average out, with models more closely following the thick ERA5 and multi-model mean lines.

Cross-equatorial AHT (AHT_{eq}) is known to correlate with the latitude of the tropical rainband (Kim et al., 2021). A 0.1 PW change in annual mean AHT_{eq} has previously been reported to correspond to a $\sim 0.5°$ shift in the zonal-mean rainband latitude under various climate forcing scenarios, e.g., Fig. 10 of Donohoe et al. (2013). Intermodel standard deviations of AHT_{eq} and the individual components are shown in Table 1, giving some quantification of the magnitude of the intermodel model differences shown in Fig. 1. In the annual mean, DJF and JJA, the latent heat component shows the largest intermodel spread, with the radiative and latent heat components showing similar-sized standard deviations in SON and MAM.

Figure 3a shows how intermodel differences in AHT_{eq} correlate to the rainband latitude (centroid and maximum) throughout the year in the *historical* simulations, and how the total AHT_{eq} correlates to each component. The precipitation centroid is statistically significantly correlated with AHT_{eq} throughout the year (Fig. 3a, left column), while for the maximum precipitation latitude correlations are generally weaker, and not significant for the annual mean or SON (Fig. 3a, second column), likely reflecting poorer representation of bimodal precipitation distributions (Donohoe et al., 2019). Although precise values vary, similar behavior is seen in the *piControl* simulations (Fig. 3b), supporting that these correlations are robust in the absence of a forced climate signal and over a longer data record. From left to right, the remaining columns in Fig. 3a show the correlation between the total AHT_{eq}, and the value attributed to each component. In DJF and JJA, the latent heat component is most strongly correlated with the total, with correlations to other components considerably weaker, despite the strong contribution of radiative fluxes to interhemispheric contrast in the multi-model mean. In the annual mean, and MAM and SON, both latent heat and radiative input attributed AHT show significant correlations with the total.

Figure 3c and d respectively show correlations between the latent heat and radiative input attributed AHT_{eq}, and the rainband latitude, total AHT, and other components. These panels highlight that the latent heat and radiative heat terms are not strongly correlated to one another, so that correlations between each term and total AHT_{eq} do not appear to arise from shared processes. The latent heat term is statistically significantly correlated with the maximum precipitation latitude in the same seasons as is the total AHT_{eq} (DJF, JJA, MAM), albeit with generally weaker correlations. However, correlations to the precipitation centroid are weak besides DJF. This term is negatively correlated with sensible heat in the annual mean and all seasons except MAM, reflecting the partitioning of turbulent energy fluxes between latent and sensible heat. The radiative input attributed AHT_{eq} (Fig. 3d) has statistically significant correlations with the precipitation centroid in all seasons except for DJF, but weak correlation to the maximum precipitation latitude, and to other terms in most seasons, with the exception of annual-mean and SON sensible heat, and DJF storage. The maximum precipitation latitude and centroid often differ from one another significantly (Fig. B1). AHT_{eq} is linked to the rainband latitude via their shared relationship to the overturning mass streamfunction. One interpretation of Fig. 3a, c and d could be that the precipitation centroid relates more closely to the overturning mass streamfunction and so AHT_{eq}, while the maximum precipitation latitude may relate more closely to cross-equatorial moisture fluxes characterized by the gradients in $P-E$, which may be partially captured by the latent heat attributed component of AHT_{eq}.

Figures B7 and B8 show equivalent figures to Figs. 1 and 3 for an alternative partitioning used in previous work, which considered absorbed shortwave (SWABS), top of atmosphere longwave (OLR), and surface heat exchange (longwave and turbulent fluxes, SE) (Donohoe et al., 2013; Kim et al., 2021). Partitioning the MSE budget in this alternative

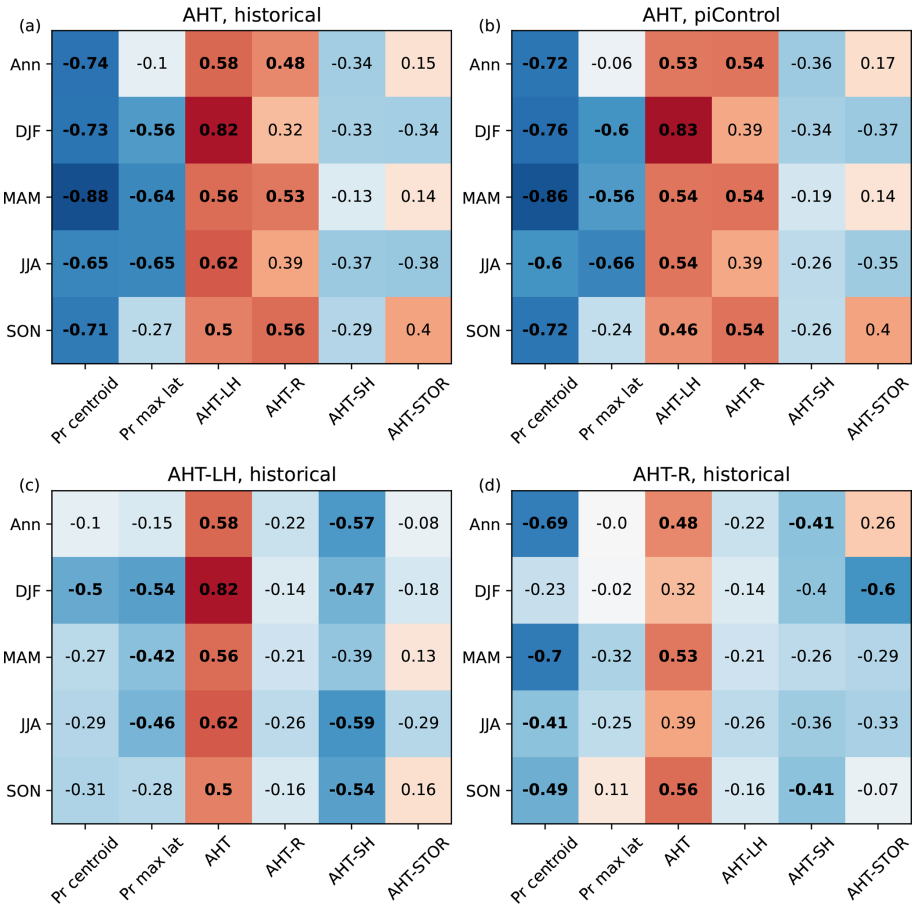

Figure 3. Top row: Pearson-r correlation between zonal-mean AHT_{eq}, and the rainband latitude (precipitation centroid and latitude of maximum) and attributed AHT_{eq} components for the *historical* **(a)** and *piControl* **(b)** simulations. Bottom row: As above, but correlating against AHT_{eq} attributed to the latent heat flux **(c)** and net column radiative input **(d)**. Colors indicate the strength and sign of the correlation, bold font shows where correlations are statistically significant ($p < 0.05$).

way yields weaker correlations of the individual components with AHT_{eq}, the precipitation centroid and the latitude of maximum precipitation.

Overall, the correlations in Fig. 3, alongside the standard deviations in Table 1, suggest a relationship between intermodel differences in interhemispheric contrasts in radiative fluxes and latent heat, and intermodel differences in total AHT_{eq} and rainband latitude. However, the correlations observed between these zonal-mean quantities could arise from a range of regional processes.

3.3.2 Regional AHT differences: Boreal summer

To explore dominant regional patterns of intermodel differences, we examine the leading order intermodel Empirical Orthogonal Functions (EOFs) of χ in JJA and DJF. EOFs 1 and 2 and regressions onto these are shown in the main text, EOF 3 is shown in Figs. B9 and B10 for JJA and DJF respectively.

Figures 4a and 5a show the first and second intermodel EOFs of χ for JJA. These intermodel EOFs explain 47.5 % and 19.0 % of the intermodel variance respectively. EOF1 shows a zonal dipole, with energy divergence from longitudes spanning the eastern Pacific, Americas and Atlantic, and energy convergence into longitudes spanning South Asia to the Central Pacific (Fig. 4a). Associated EFEs and EFPMs are also plotted for Figs. 4 and 5, showing the shift when $2\times$ the pattern in panel (a) of each is added to (gold), or subtracted from (black), the multi-model mean χ. For Fig. 4a, the magnitude of this addition or subtraction is similar to that of the difference in χ seen between El Niño and La Niña conditions in reanalysis (Boos and Korty, 2016). These indicate that EOF1 links to substantial east-west shifts in the EFPM over Asia. Zonally varying EFE shifts are also seen, specifically a northward EFE shift over Asia and Africa, and a southward shift over the Pacific and Americas. Figure 4i shows the associated precipitation changes, which include a westward shift over Asia, consistent with the EFPM shift towards the west, and a southward shift over the Pacific, con-

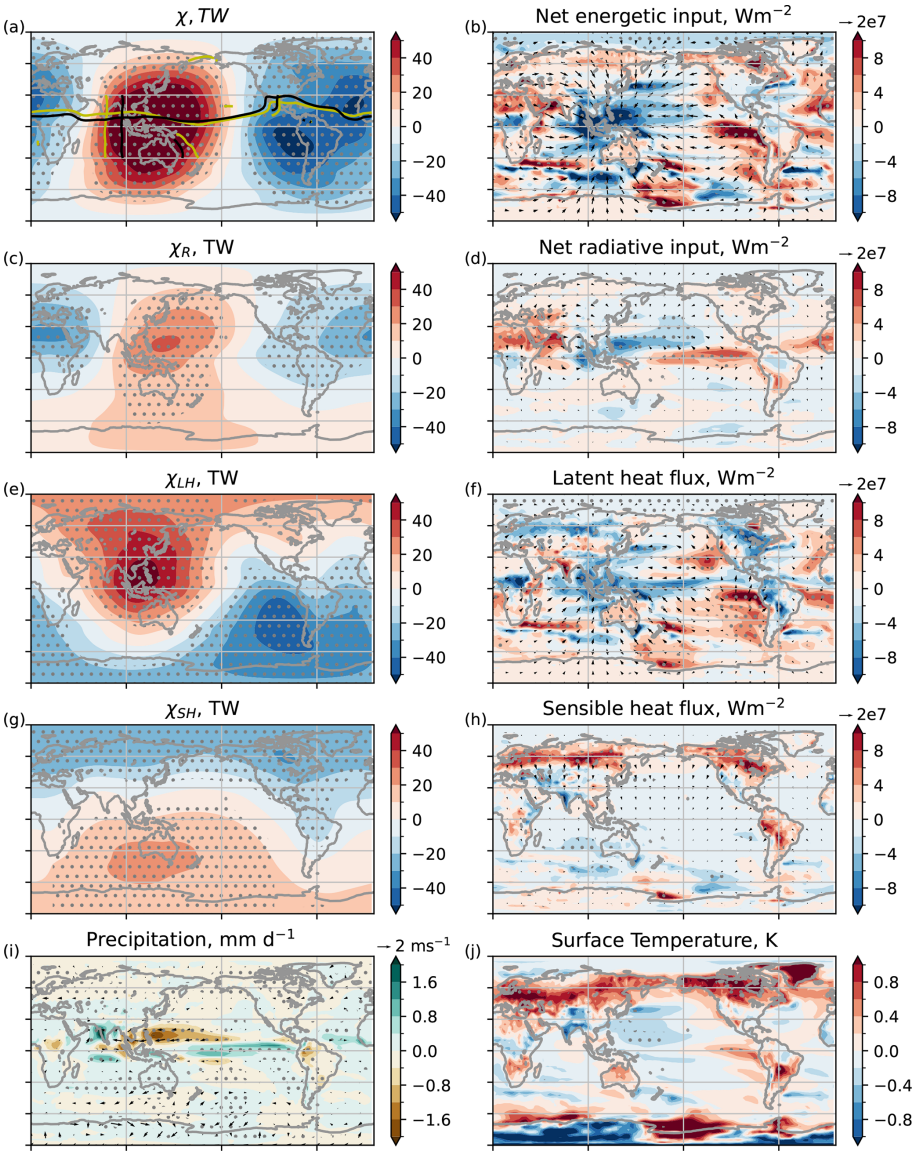

Figure 4. Intermodel covariance between JJA PC1 (scaled to unit variance) and variables of interest. Panel **(a)** shows EOF1 of χ, panel **(b)** shows the vertically integrated, divergent MSE transport (arrows) and the net column energetic input (colors). The lines in panel **(a)** show the EFE and EFPM when $2\times$ the χ pattern shown added to (gold) or subtracted from (black) the multi-model mean χ. $2\times$ is chosen to help visibility of features on the figure. Subsequent rows show (left) the components of χ and (right) the associated MSE transport (arrows) and column energy input (colours). Panel **(i)** shows precipitation and 850 hPa wind vectors, panel **(j)** shows near-surface air temperature. Stippling indicates statistical significance for the variable shown in colors, defined as where the p-values for the correlations pass a false discovery rate of 0.15 (see Wilks, 2016).

sistent with the EFE shift. Meanwhile, EOF2 (Fig. 5a) shows a pattern reflecting interhemispheric contrast, with enhanced energy transport from the Southern to the Northern Hemisphere. EOF2 links to zonally consistent north-south EFE and precipitation (Fig. 5i) shifts that have more widely been considered in the energetic framework.

The remaining panels in Figs. 4 and 5 show regressions of the fluxes and near-surface air temperature onto the associated principal component (PC). EOF1 reflects strong intermodel differences in energy convergence over the Western Pacific warm pool and Maritime Continent, with divergence from other regions (arrows in Fig. 4b), including a maximum over the Eastern Pacific cold tongue (Fig. 4a). To interpret this pattern, we look first at temperature. A positive-signed PC1 is correlated with warmer surface temperatures across much of global land, cooler temperatures over the Western North Pacific, and a warmer Pacific cold tongue (Fig. 4j). The overall picture is of enhanced thermal contrast between

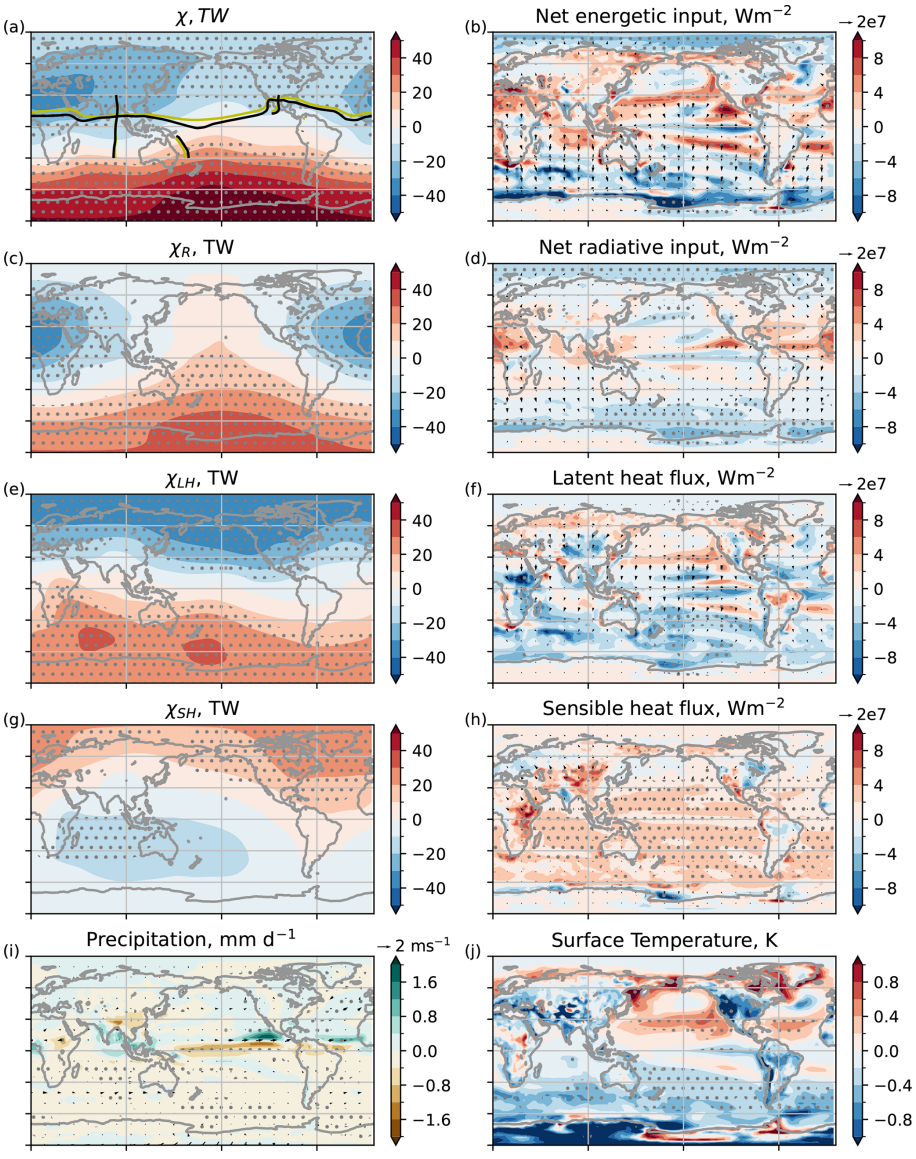

Figure 5. As Fig. 4 but for JJA PC2.

land and sea, and across the Pacific. This is accompanied by easterly anomalies over the western Pacific, which correspond to a weakening in magnitude of the monsoon westerlies up to the Philippines, and a strengthening of the trades over the Western Pacific. Fully determining the causal relationship between these wind anomalies, the surface temperature, and the latent heat flux is beyond the scope of this paper, but we briefly consider plausible mechanisms here. Tuckman et al. (2024) describe a monsoon mode whereby advection of warm, moist air by monsoon westerlies leads to warming of the ocean surface due to suppressed sea surface cooling by turbulent fluxes. Consistent with this, for negative PC1 values, from Fig. 4 we see that EOF1 would show an association of extended monsoon westerlies with weakly warmer surface temperatures. However, here this would be associated with an enhanced, rather than suppressed, turbulent latent heat flux (Fig. 4f). We find that a similarly structured EOF1 dominates the intermodel spread in χ in AMIP simulations where there is no coupled ocean (not shown), suggesting that the intermodel differences seen here may be predominantly due to differing parameterizations of turbulent heat fluxes or convection, rather than atmosphere-ocean coupling, with a particularly pronounced impact on the net energetic input over the warm pool.

The reduced latent heat flux over the Western Pacific appears to contribute to reduced humidity, and weakened precipitation over the Western North Pacific. Strengthened outgoing longwave radiation (OLR) associated with the reduced rainfall results in the negative net radiative input signal seen in Fig. 4d. Similarly, regions of stronger precipitation and re-

duced OLR over the Pacific and Atlantic link to enhanced radiative input. This suggests that the radiative input changes are more a result of rather than energetic cause of the rainband shifts, although they may act as a feedback onto the observed shifts. Maxima in χ_R and χ_{LH} align with the reduced energetic input from latent heat and radiation over East Asia and the Western Pacific, and both support the overall pattern seen in χ. The minimum in χ_{LH} aligns with the enhanced NEI associated with stronger evaporation over the warmer Pacific cold tongue (Fig. 4e, f), which in turn links to a minimum in χ in this region (Fig. 4a, b).

Enhanced land-sea temperature contrast associated with EOF1 stands out in (Fig. 4j). This may contribute to altered divergence and convergence of energy linked to shifts in stationary circulation patterns, although such shifts are not obvious from wind anomalies (Fig. 4i). However, the low heat capacity of the land surface means that these temperature anomalies generally do not map to strong changes in column energy input over land (Fig. 4b). In many land regions, warmer near-surface air temperatures are associated with a reduced latent heat flux and a compensating enhanced sensible heat flux, particularly over northern Eurasia and the Americas (Fig. 4f, h). This pattern suggests land-surface warming in models with weaker evapotranspiration. In the NEI, these fluxes compensate, leaving a weak increase in NEI over higher latitude land (Fig. 4b). Warmer temperatures over northern Africa and the Middle East instead relate to enhanced humidity and shortwave absorption (not shown). This drives NEI to the atmosphere over this region (Fig. 4b) and supports a minimum in χ over northern Africa (Fig. 4a and c).

While EOF1 relates chiefly to land-sea/east-west thermal contrasts, EOF2 describes north-south thermal contrasts. Models with PC2 positive tend to have cooler Southern Ocean temperatures, and a northward shift of the rainband over the Atlantic and Pacific (Fig. 5a, i and j). Similarly to EOF1, both the radiative input and latent heat flux components show significant contributions to this mode in the breakdown of χ (Fig. 5c and e), with both showing clear interhemispheric contrast. The cooler Southern Ocean temperatures are associated with reduced Southern Ocean net radiative input due to weaker upward surface longwave fluxes, and reduced latent heat flux due to weaker evaporation over cooler water. Both of these effects support the overall pattern of enhanced interhemispheric contrast in NEI, and the associated EFE shifts. The Southern Ocean is a known region of SST bias, with CMIP models on average having a too-warm Southern Ocean. Intermodel differences may relate to differing representation of the processes governing Southern Ocean SST that lead to this too-warm multi-model average bias. In CMIP5 the warm bias was suggested to relate to errors in the Atlantic Meridional Overturning Circulation (Wang et al., 2014), or shortwave cloud radiative effects (Hyder et al., 2018). However, a more recent analysis of CMIP6 suggested a relationship to warm biases in the North Atlantic deep ocean (Luo et al., 2023).

The radiative input attributed component additionally shows a region of enhanced energy divergence, and associated net radiative input (Fig. 5d), which extends across northern Africa, from the Atlantic to central Asia. This relates to enhanced shortwave absorption over northern Africa and the Middle East due to increased humidity, alongside reduced outgoing longwave over regions of enhanced precipitation in the Atlantic and eastern Pacific (not shown).

3.3.3 Regional AHT differences: Austral summer

Figure 6a shows EOF1 of χ for DJF (48.2 % of variance). Similar to EOF1 for JJA, the mode links to enhanced zonal energy transport across the Pacific. The dipole shows a slight westward shift in DJF compared to JJA, with a stronger relationship with cold pool net energy input and a weaker relationship with radiative effects over North Africa and the Middle East (Fig. 6b vs. Fig. 4b). The maximum of the dipole still appears primarily anchored to intermodel differences in warm pool net atmospheric energy input. This EOF is associated with warmer temperatures across Africa, Asia and South America, as well as the Nino1+2 and 3 regions. This EOF broadly resembles the pattern in χ seen under ENSO in ERA-Interim reanalysis data (Boos and Korty, 2016), including an eastern shift in the western Pacific EFPM and a western shift in the EFPM over the Americas for warmer eastern Pacific temperatures. Note that the difference in longitude between the climatological EFPM in JJA relative to DJF (Boos and Korty, 2016; Tuckman et al., 2024) yields an opposite signed shift in the EFPM between JJA and DJF for the same sign of this dipole. Precipitation shows an enhanced double-ITCZ structure, with weakened rainfall over the equator accompanied by enhanced rain north and south of the equator over the western Pacific. There is also weakly enhanced precipitation over southern Africa.

This mode links to enhanced evaporation over the Eastern Pacific, perhaps linked to warmer water over the cold tongue. Reduced evaporation is seen over Southern hemisphere and low latitude land, and over the SPCZ and Western North Pacific. Sensible and latent heat anomalies again oppose one another over land, and suggest drier, warmer land when PC1 is positive (Fig. 6f, h). In contrast to JJA, over subtropical land the net effect is of these compensating turbulent fluxes is reduced NEI (Fig. 6f). Net radiative input again broadly reflects changes to the rainband structure, suggesting that this supports but does not itself drive the observed shifts (Fig. 6d). Discerning likely drivers and consequences of the altered latent heat flux would need targeted simulations within a single model, e.g. perturbed parameter or altered SST simulations, and is beyond the scope of this paper. However, as with JJA, it can be seen that the latent heat flux term is dominant in the partitioning of χ into components (Fig. 6e), indicating

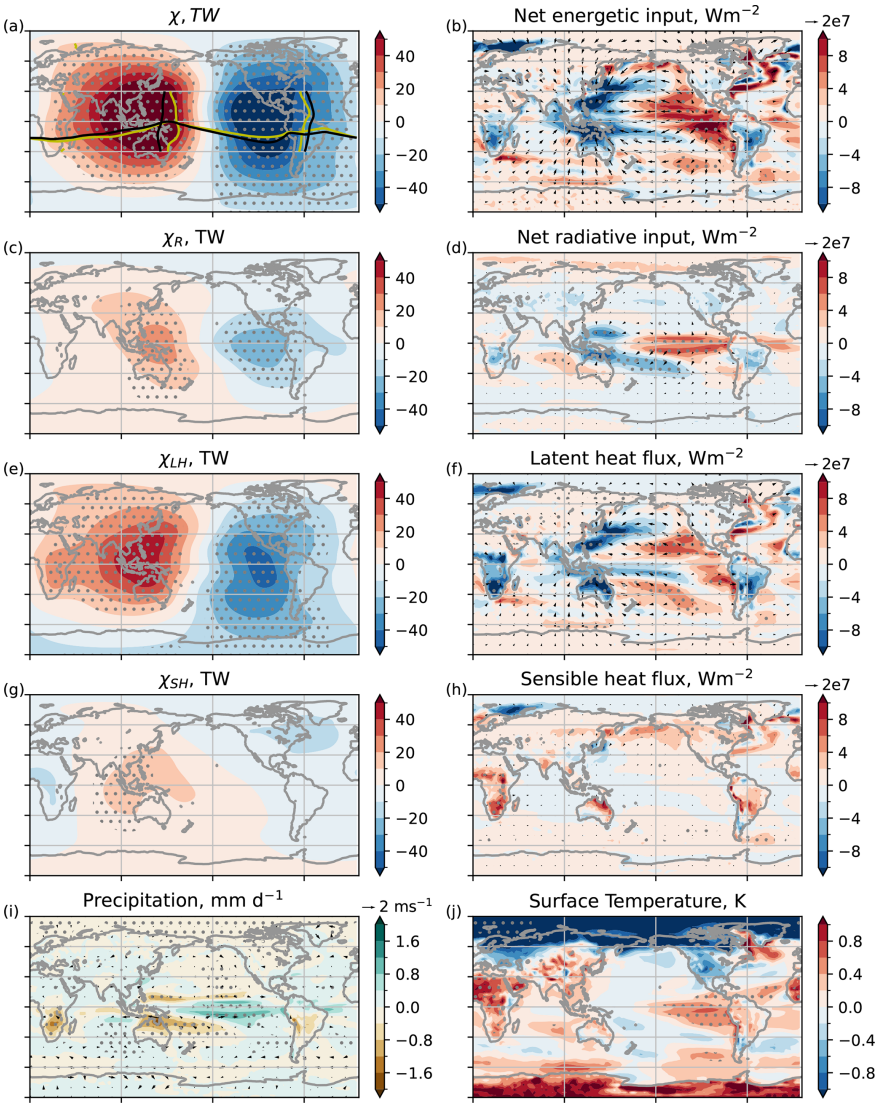

Figure 6. As Fig. 4 but for DJF PC1.

that these latent heat differences are an important signature of intermodel differences in divergent energy transport.

Similar to JJA, EOF2 for DJF (21.2 % of variance) shows a mode linked to interhemispheric thermal contrast and SST anomalies over the Southern Ocean (Fig. 7j), although this season shows a more pronounced zonal structure, with a minimum of χ over the Pacific. The latent heat flux component strongly dominates this mode, with most of the spatial structure of the NEI and χ reflecting that of the latent heat flux and χ-LH (Fig. 7a, b, e and f). Enhanced latent heat flux occurs over warmer water, with weaker latent heat flux over cooler Northern Hemisphere ocean regions and land. This mode correlates to a weak southward shift in precipitation across the Pacific and Atlantic, associated with generally cooler global land, and a warmer Southern Ocean. Pronounced latent and sensible heat fluxes are seen over western boundary current regions, with the same sign for both fluxes, in contrast to the opposing relationship seen in Fig. 3. Changes to radiative fluxes are weak compared to other EOFs, and at low latitudes broadly align with precipitation changes (Fig. 7d, i).

3.4 Energetic pathways of bias and change

Having examined the structures of the leading EOFs describing the intermodel differences, we now use PCs to visualize these differences in a lower dimensional space, and to explore how the position in PC space reflects differences in the latent and sensible heat, radiative fluxes, and storage. The aim is to diagnose intermodel differences and identify similar behaviors between models. Intermodel differences can arise through a range of differences in convection, turbulence, circulation, etc., and we do not causally attribute these differences to a particular term in the MSE budget. Note also that

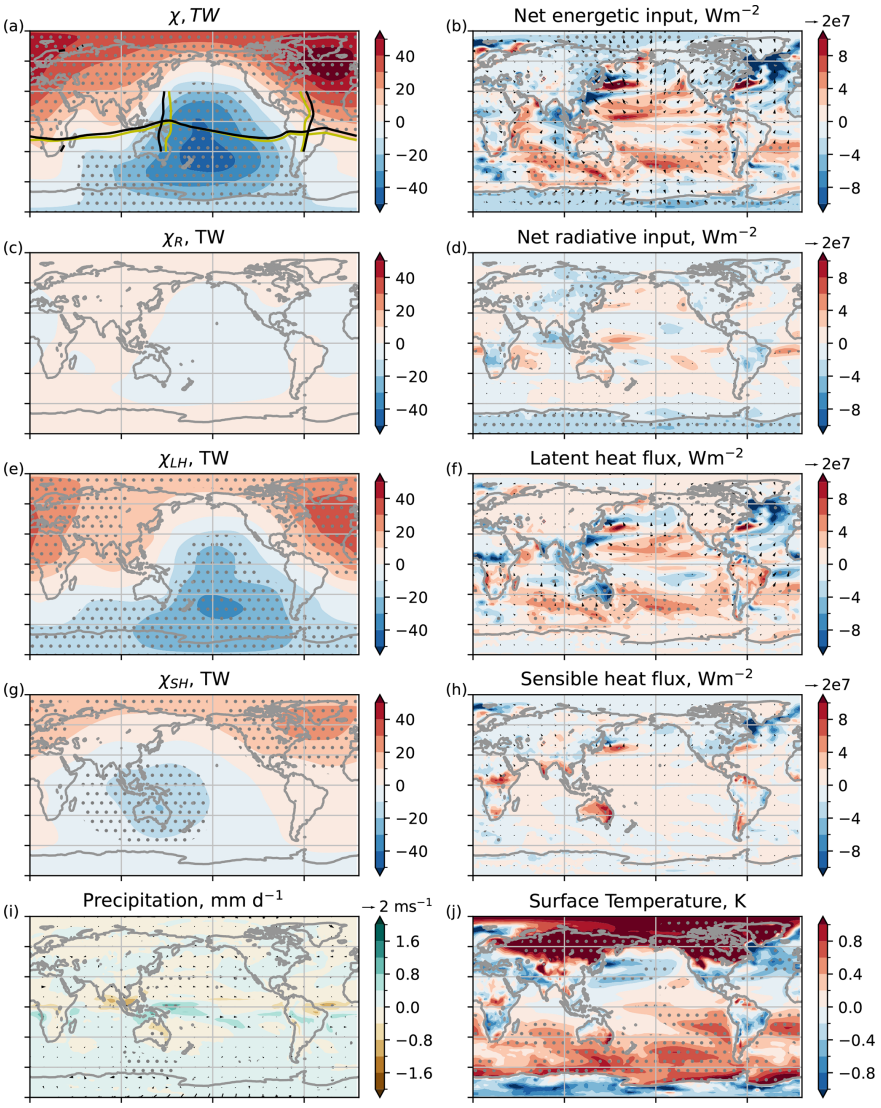

Figure 7. As Fig. 4 but for DJF PC2.

we do not mean to imply a physical linkage between the historical JJA intermodel spread and future climate change responses, but only to use this as a low-dimensional basis to visualize the different model responses.

Figure 8 shows scatter plots of the values of PC1 versus PC2 for each model used in the EOF analysis for JJA (left) and DJF (right). Travel from left to right along the x-axis indicates the multiplier onto EOF1, e.g. a strong positive value would indicate a stronger enhancement of energy import into the Western North Pacific from other regions (cf. Fig. 4). Travel from bottom to top along the y-axis similarly indicates the multiplier onto EOF2, i.e. enhanced MSE transport from the summer to the winter hemisphere. As would be expected, models from the same modeling center tend to be located near to one another in the PC space, for example the HadGEM and UKESM models. ERA5 PCs are marked by crosshairs for comparison, and $(0, 0)$ corresponds to the multi-model mean.. For JJA, a cluster of models that includes CanESM5, INM-CM5-0, EC-Earth3, CMCC-ESM2 and MPI-ESM1-2-HAM sits closest to the ERA5 value. In DJF, models are slightly more evenly spread in PC space, and ACCESS-ESM1-5, CMCC-ESM2, INM-CM5-0 and MIROC-ES2L sit closest to the ERA5 values. However, note that this figure neglects higher order PCs, and that compensation between components (discussed below) can mask biases, so models closer to the ERA5 cross-hairs are not necessarily more skillful. Given some similarities in their spatial patterns (Figs. 4 to 7), it is interesting to ask how the seasonal PCs relate to one another. We find a weak correlation between PC1 in JJA and DJF (Pearson's $r = 0.27$, $p = 0.1$). Similarly, PC2 between the two seasons shows a weak correlation, with a Pearson's r of 0.31 ($p = 0.05$). No significant

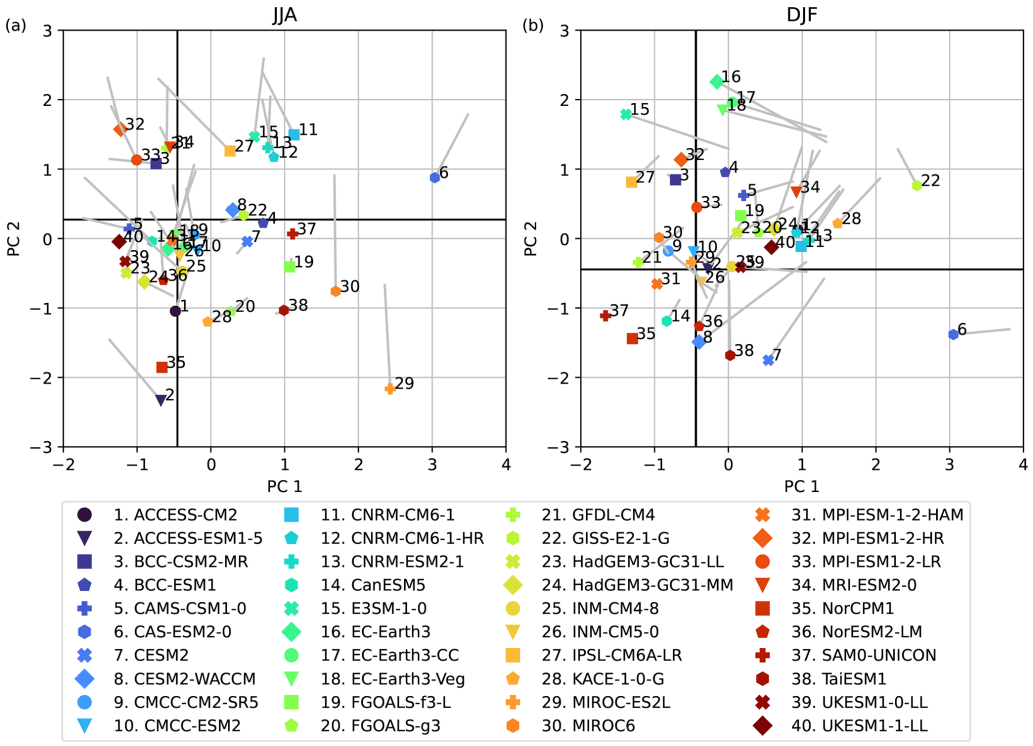

Figure 8. Scatter plot showing PC1 vs PC2 for **(a)** JJA and **(b)** DJF. Symbols show the values of each for the *historical* simulation. Grey lines extend from each symbol to the new PCs when χ from the *SSP5-8.5* simulation (where available) is projected onto the *historical* EOFs. Black vertical and horizontal lines indicate the PC1 and 2 values obtained when ERA5's χ is projected into this space. In both seasons a positive PC1 indicates energy import into the Western North Pacific. A positive PC2 indicates enhanced MSE transport from the summer to the winter hemisphere, i.e. a cooler (warmer) Southern Hemisphere in JJA (DJF).

correlations (at $p = 0.1$) are found between PC1 and PC2 across different seasons.

The gray line from each model shows the trajectory in the PC space from a given *historical* simulation to end-of-century climate in the *SSP5-8.5* simulation, with PCs obtained by projecting the *SSP5-8.5* χ onto the *historical* χ EOFs, having first removed the *historical* multi-model mean. In JJA (Fig. 8a), the majority of models undergo an increase in PC2 under global warming, suggesting enhanced southward interhemispheric energy transport. Shifts in PC1 are generally smaller and more varied, with no obvious pattern in the sign or magnitude of shifts related to their initial location in PC space. In DJF (Fig. 8b), the majority of models undergo an increase in PC1 under warming, consistent with a shift towards warmer eastern Pacific SSTs (Collins et al., 2010). Shifts in PC2 are more varied, with most models undergoing a positive shift, suggesting enhanced northward interhemispheric energy transport. Again, we also test correlations between the *SSP5-8.5-historical* changes in PC1 and 2 for JJA and DJF. For PC1, JJA and DJF indices correlate with a Pearson's r of 0.39 ($p = 0.02$), so that, for example, enhanced warm pool convection in JJA under SSP5-8.5 links to similar DJF changes. For PC2, Pearson's r is -0.55 ($p = 0.001$), suggesting that, for example, models with enhanced northern to southern hemisphere JJA AHT have weaker southern to northern hemisphere DJF AHT. This may reflect known intermodel differences in the changes in annual-mean interhemispheric thermal contrast (Chen et al., 2022). Correlations between PC1 and PC2 between seasons are weak and not statistically significant.

The total AHT and χ can be partitioned into the four terms considered throughout this paper (net radiative input, latent and sensible heat fluxes, column storage). Figure 9 shows the projections of the χ components for each of these terms into the EOF space for JJA. This provides insight into how different terms contribute to a given model's overall location in the PC space, and which terms cancel one another. It is important to note that causally, these differences can arise from a range of different processes in the models, rather than being fundamentally driven by one of these terms. Instead, this approach provides a summary metric to diagnose how models differ, and to identify models that may behave in similar ways to one another. As the energy budget for ERA5 does not close (see "Methods"), a similar decomposition is not possible for ERA5. Figures 4–7 indicated a combined role for the radiative and latent heat components in contributing to the overall patterns of intermodel difference in χ. Figure 9 highlights that for some models these terms do act in combination, e.g.

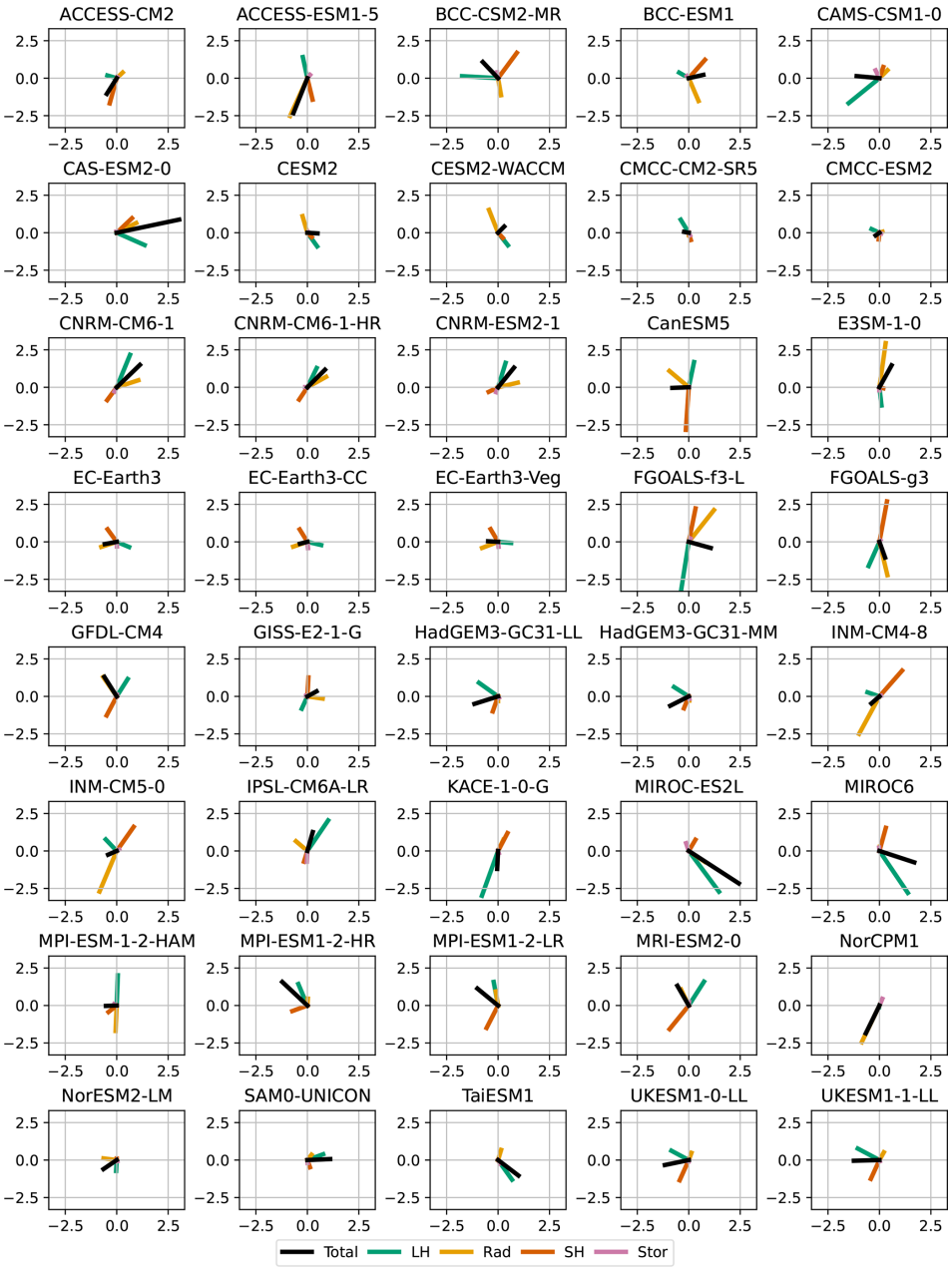

Figure 9. Symbols show each model's location in JJA PC space, matching those in Fig. 8. Black lines show the total difference relative to the multi-model mean $(0, 0)$ as a vector. The remaining lines show the breakdown of how this total difference arises in terms of latent heat (green), sensible heat (red), radiative input (orange) and storage (pink).

the CNRM model family, but for other models they may act in opposition, with one or the other dominating the overall structure of χ, e.g. ACCESS-ESM1-5 vs. KACE-1-0-G.

Figure 9 demonstrates that some models appear in almost the same location in PC space via different processes. For example, Fig. 10 shows JJA χ and its breakdown for EC-Earth3 and MPI-ESM-1-2-HAM, relative to the multi-model mean. These models also have similar values for higher PCs (not shown). MPI-ESM-1-2-HAM has a very similarly structured χ to EC-Earth3, with similarly located EFE and EFPMs. In EC-Earth3, this structure arises predominantly from the radiative contribution to χ. However, for MPI-ESM-1-2-HAM there is cancellation between a strong PC2 radiative and latent heat flux terms, and the overall structure arises as a combination of the residual of this cancellation, alongside the sensible heat flux term. For the *historical* simulations, Fig. 9 demonstrates that various pathways exist by which a model can achieve a given χ, and so EFE/EFPM location, although

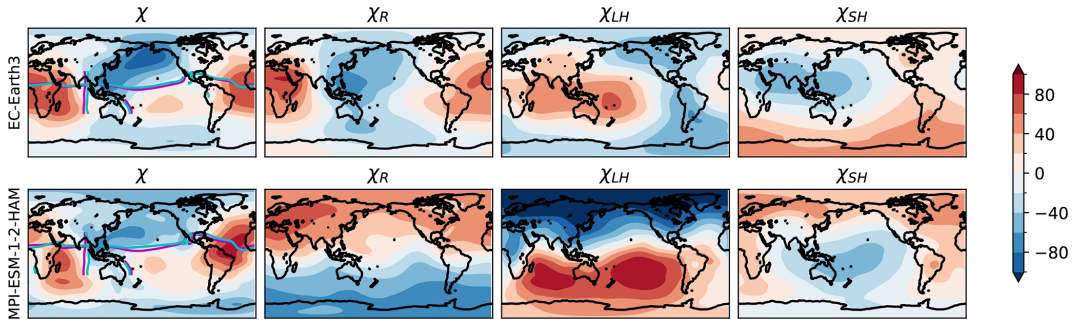

Figure 10. Comparison of the total difference of JJA χ relative to the multi-model mean for two models with similar values of PC1 and 2: EC-Earth3 (top) and MPI-ESM-1-2-HAM (bottom). Left column shows χ, alongside the models' EFE and EFPM in cyan. Magenta lines show the multi-model mean EFE and EFPM. From left to right, the remaining columns show the decomposition of χ into radiative input, latent heat, and sensible heat.

it is usually models from the same family that follow similar pathways.

Figure 11 shows the breakdown of the shift in JJA PC space from the *historical* to the *SSP5-8.5* simulation. Some similarities are evident across models as the climate warms. For all models the latent heat contribution is directed with PC1 negative, relating to generally weaker increasing, or decreasing evaporation over many land regions compared to ocean. For most models the latent heat PC2 is also negative, relating to enhanced ocean evaporation between 0 and −30°, and particularly over the Indian Ocean, Maritime Continent and western Pacific. For all models sensible heat has PC1 and PC2 positive, linked to warming of land relative to ocean. The storage term is larger than for the *historical* simulations, and usually takes a sign in negative PC2, likely indicating warming of the Northern Hemisphere relative to the southern in JJA. In contrast, the sign of the radiative term varies across models, perhaps related to intermodel differences in the distribution of cloud cover and water vapor. However, despite radiation showing perhaps the greatest intermodel differences in sign, none of these individual terms clearly dominates the intermodel differences in total χ, which is instead arises from the combination of terms.

Within the shifts shown in Fig. 11, some similar storylines now appear in different model families, for example HadGEM3-GC31-MM and KACE-1-0-G. In order to group together models with similar changes in both χ and the relevant fluxes, we apply hierarchical clustering using 12 values as features: the first 3 PCs of total χ, and the first 3 pseudo-PCs of the breakdown of χ by latent heat, sensible heat and radiative input (see Fig. B9 for JJA's PC3). The resulting dendrogram is shown in Fig. B11. Based on this, we identify groups of models with shared climate change energetic storylines in χ. Figure 12 shows χ for 3 pairs of models from Fig. 11, providing examples of some of these distinct patterns of change. The multi-model mean difference is shown in the bottom row for comparison. Figure B12 shows the associated column energy input for each component of χ.

HadGEM3-GC31-MM and KACE-1-0-G illustrate one storyline. Here, a strong reduction in radiative input over the Maritime Continent and Indian Ocean is partially balanced by enhanced evaporation in these regions. Broader scale enhancement of evaporation across the low latitude Southern Hemisphere ocean, relative to the Northern Hemisphere, supports a southern shift of the EFE across the Pacific. In contrast, in CAMS-CSM1-0 and INM-CM4-8, stronger evaporation the over Indian Ocean and Western Pacific versus the Eastern Pacific leads to a pronounced PC1 structure to the latent heat component of χ. In these models, the change in net radiative input is weak, and reduced input over the Indian Ocean does not compensate enhanced evaporation, leading to an overall PC1 pattern in the opposite sense to that of KACE-1-0-G and HadGEM3-GC31-MM. Changes in both the EFE and EFPM in these models are relatively weak.

In the above models, the latent heat and radiative terms work generally in opposition to one another in their contributions to χ. In IPSL-CM6A-LR and CanESM5, rather than these terms being zonally in antiphase with one another, their peaks are offset by $\sim 90°$. In these models, there is an increase in net radiative input over the northern Pacific, leading to a strong minimum in χ. However, there is also a strong enhancement of evaporation over the Indian Ocean and South Pacific Convergence zone, leading to a secondary minimum in χ. Reduced evaporation and net radiative input over South America and the Atlantic result in a maximum in χ. These models show a similar southward shift in the EFE over the Pacific and eastward shift in the EFPM over South Asia to that seen in KACE-1-0-G and HadGEM3-GC31-MM, despite the differently structured χ changes. Understanding how these different but consistent combinations of terms arise is left for future work, but could give useful insight into storylines of AHT and tropical rainfall change.

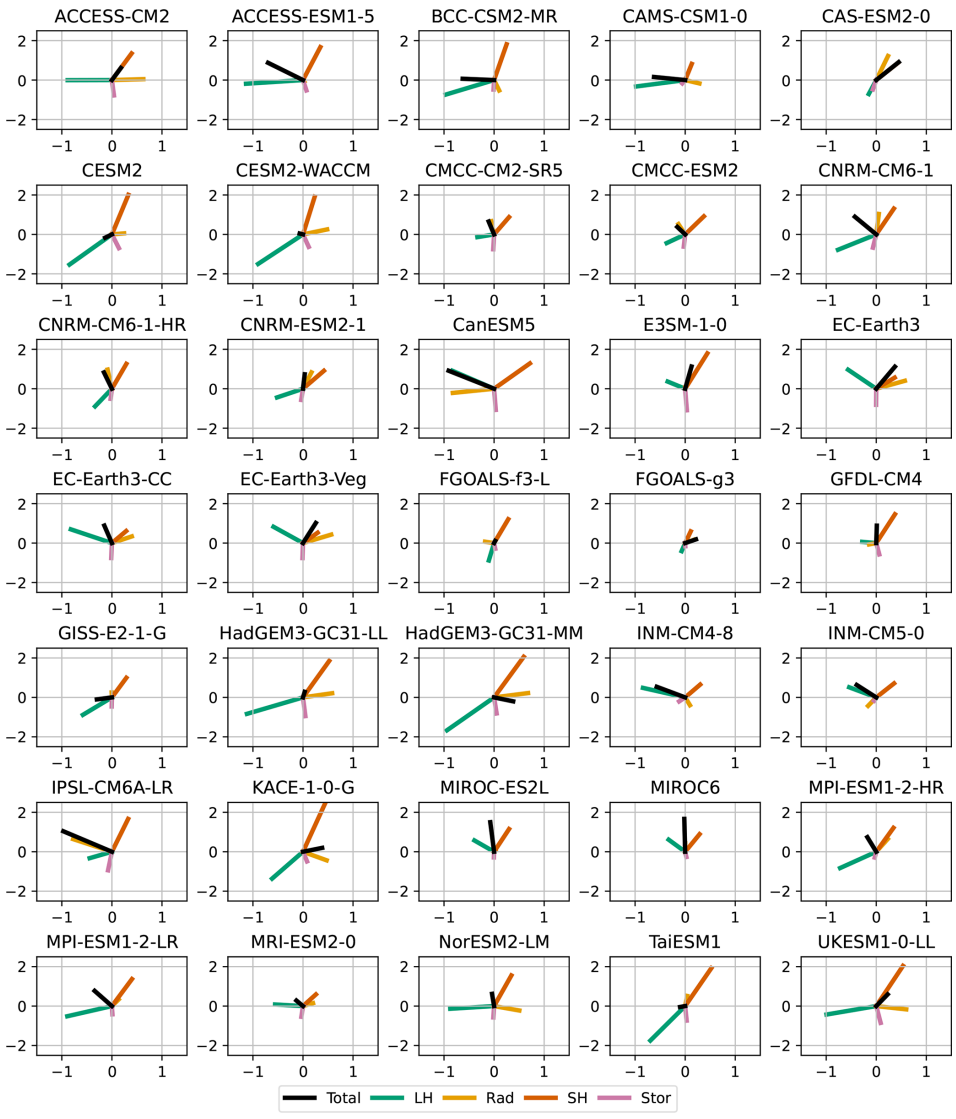

Figure 11. A breakdown of the shifts in JJA PC1 and 2 under *SSP5-8.5*, relative to the model's *historical* simulation, which is here centered at $(0, 0)$. Black lines show the total difference between *SSP5-8.5* and the *historical* simulation as a vector in PC space. The remaining lines show the partitioning of this total response in terms of latent heat (green), sensible heat (red), radiative input (orange) and storage (pink).

4 Conclusions

The EFE has been used to interpret the location of the ITCZ, but its behavior is known to differ between models, and in response to forcings such as greenhouse gases (Biasutti et al., 2018). In this study, we used the Energy Flux Potential, χ, to explore seasonal and regional behavior in CMIP6, and intermodel differences in both *historical* and *SSP5-8.5* simulations from CMIP6. By partitioning the atmospheric heat transport into radiative fluxes, latent and sensible heat, and storage, we identify pathways via which differences in the EFE and EFPM could arise. On seasonal timescales, in the zonal mean, we find a similar result to that for the annual-mean (Fajber et al., 2023), where the overall structure of total divergent AHT strongly resembles the latent-heat-attributed component, with radiative-flux-attributed transport linked to the sign at the equator (Fig. 1).

Regionally, the picture is more complex. Radiative heating and latent heat fluxes remain the dominant terms in the MSE budget. In DJF the spatially varying perspective is broadly similar to that suggested by the zonal-mean. Land-sea constrasts in latent heat fluxes appear to govern the zonal structure of χ, and consequently the AHT, while radiative heating introduces interhemispheric contrasts. In JJA, the warming of the Northern Hemisphere land surface instead leads to stronger zonal contrasts in the radiative heating contribution, so that both radiative fluxes and latent heat make a clear contribution to the overall spatial structure of χ. These

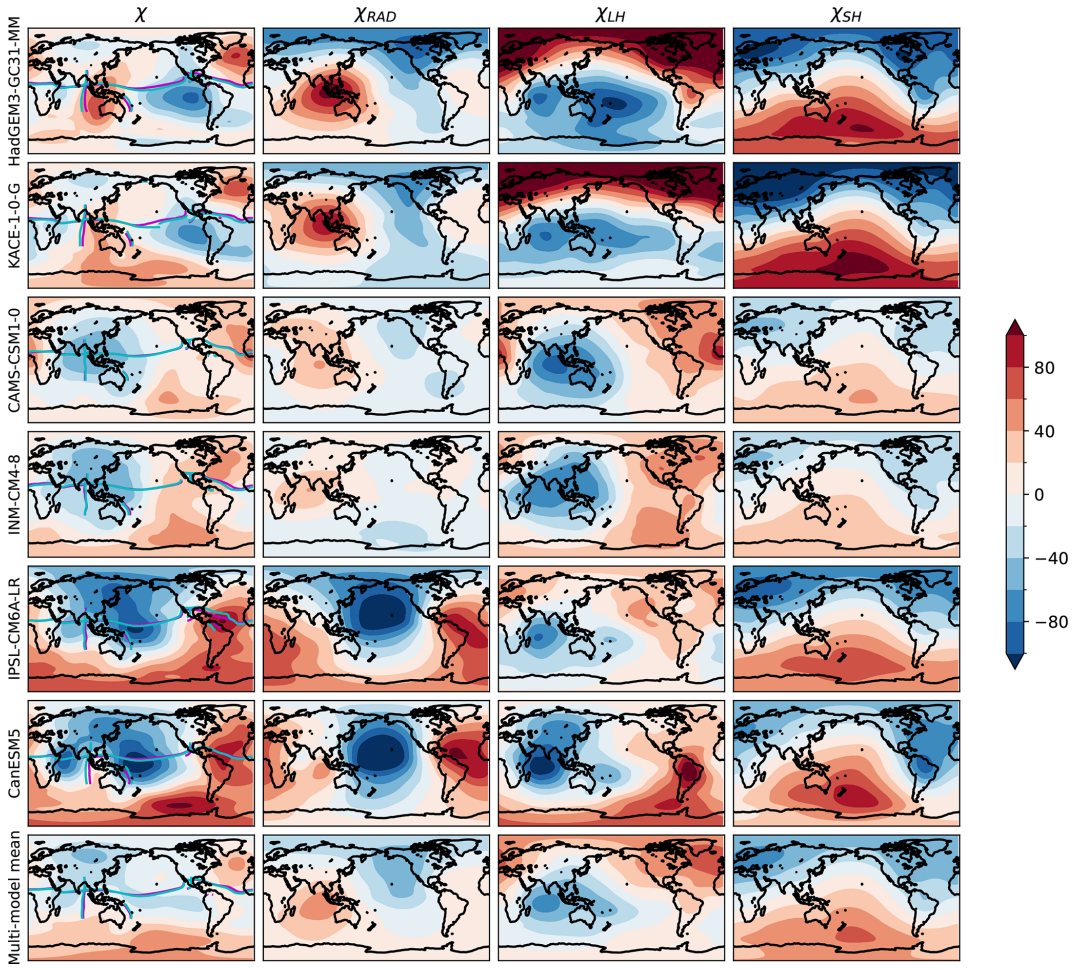

Figure 12. Changes in χ and its components at end-of-century in *SSP5-8.5* relative to the *historical* simulation for JJA. Three pairs of models following similar storylines are shown. The bottom row shows the multi-model mean difference for the 35 models for which *SSP5-8.5* data was available. Left column shows χ, alongside the models' *SSP5-8.5* and *historical* EFE and EFPM in cyan and magenta respectively. From left to right, the remaining columns show the partitioning of χ into radiative input, latent heat, and sensible heat.

results suggest that latent heat is important in communicating the TOA radiative imbalance that governs AHT to the atmosphere, although we note that the latent heating itself is in balance with the broader circulation, which maintains the surface conditions that determine evaporation.

Intermodel EOFs show that in both JJA and DJF, the dominant mode of intermodel difference in χ is a zonal dipole, which relates to shifts in the EFPMs, and localized shifts in the EFE (Figs. 4 and 6). In both seasons this mode appears linked to east-west thermal contrast across the Pacific and associated patterns in evaporation, precipitation and radiative fluxes. Land-sea temperature contrast is also associated with EOF1 in both seasons, although the contribution of this to the AHT is unclear, as there is a compensation between dry and latent fluxes over the land surface with changes in temperature. Meanwhile, the second EOF in both seasons corresponds to interhemispheric thermal contrasts, which have been more widely considered in relation to ITCZ shifts. In both seasons, this mode seems particularly linked to Southern Ocean temperatures, with enhanced evaporation over warmer Southern Ocean water. In all EOFs presented, the pattern of radiative fluxes appears strongly linked to changes in OLR relating to precipitation shifts, suggesting this contribution to χ may arise as a feedback onto shifts introduced by other processes.

Mapping out different models in the PC space associated with the intermodel EOFs provides a concise way to visualize their differences in zonal and meridional AHT structure (Fig. 8). By breaking down the PCs into their components relating to radiative heating, latent and sensible fluxes, and storage, we can further reveal differences between models' overall AHT structures. This approach has potential to help to unpick compensating biases, which, as demonstrated in Fig. 10, can lead to models appearing to have similar Energy Flux Potentials, despite different causes.

When applied to change, this PC decomposition approach reveals different energetic storylines through which models response to greenhouse gases, illustrated in Fig. 12. We find that under *SSP5-8.5*, most models show a shift towards enhanced interhemispheric contrast in JJA and enhanced ENSO-like meridional contrast in DJF. These changes link to different dominant balances in different models. No single term consistently aligns with the overall changes observed, but from the models examined in Fig. 12, differences in radiative fluxes, particularly over the central Pacific, appear important in JJA. Figure 8 also suggests that the bias in χ in the *historical* simulation is not a good predictor of a model's future change, with no clear patterns apparent that might support an emergent constraint. Based on analysis of simulations from a gray radiation aquaplanet (Vallis et al., 2018), and a fully parameterized atmospheric model coupled to a slab ocean (CAM4), previous work (Fajber et al., 2023) suggested that the AHT response to increased CO_2 is mediated through evaporation in the zonal and annual mean. Our results show that on a regional scale, this picture becomes more complex.

We identify and discuss several energetic storylines of response to *SSP5-8.5* in this study. Models show inconsistent changes in χ under warming, with the breakdown by terms suggesting significant structural differences linked to radiative fluxes. This spread may link to the diversity of precipitation shifts that have been noted (Chadwick et al., 2013). It remains to be understood how these storylines are ultimately driven, e.g. for a particular storyline, which forcings or model parameterizations lead to the pathway observed, and are these drivers consistent between models that follow that storyline. Such questions could be addressed through targeted model simulations, for example altering surface properties to change evaporation, altering cloud characteristics, or changing deep entrainment profiles to alter tropical relative humidity and consequently radiation. Overall, we propose that the approach to comparing the energetic responses to greenhouse gases across models that is presented here could prove valuable in understanding the diversity of EFE and ITCZ responses to climate change.

Table A1. Summary of CMIP6 simulations used in this study.

Model name	*historical*	*piControl*	*SSP5-8.5*
ACCESS-CM2	r1i1p1f1	r1i1p1f1	r1i1p1f1
ACCESS-ESM1-5	r1i1p1f1	r1i1p1f1	r1i1p1f1
BCC-CSM2-MR	r1i1p1f1	r1i1p1f1	r1i1p1f1
BCC-ESM1	r1i1p1f1	r1i1p1f1	
CAMS-CSM1-0	r1i1p1f1	r1i1p1f1	r1i1p1f1
CAS-ESM2-0	r1i1p1f1	r1i1p1f1	r1i1p1f1
CESM2	r4i1p1f1	r1i1p1f1	r4i1p1f1
CESM2-WACCM	r1i1p1f1	r1i1p1f1	r1i1p1f1
CMCC-CM2-SR5	r1i1p1f1	r1i1p1f1	r1i1p1f1
CMCC-ESM2	r1i1p1f1	r1i1p1f1	r1i1p1f1
CNRM-CM6-1	r1i1p1f2	r1i1p1f2	r1i1p1f2
CNRM-CM6-1-HR	r1i1p1f2	r1i1p1f2	r1i1p1f2
CNRM-ESM2-1	r1i1p1f2	r1i1p1f2	r1i1p1f2
CanESM5	r1i1p1f1	r1i1p1f1	r1i1p1f1
E3SM-1-0	r1i1p1f1	r1i1p1f1	r1i1p1f1
EC-Earth3	r1i1p1f1	r1i1p1f1	r1i1p1f1
EC-Earth3-CC	r1i1p1f1	r1i1p1f1	r1i1p1f1
EC-Earth3-Veg	r1i1p1f1	r1i1p1f1	r1i1p1f1
FGOALS-f3-L	r1i1p1f1	r1i1p1f1	r1i1p1f1
FGOALS-g3	r1i1p1f1	r1i1p1f1	r1i1p1f1
GFDL-CM4	r1i1p1f1	r1i1p1f1	r1i1p1f1
GISS-E2-1-G	r1i1p1f2	r1i1p1f1	r1i1p1f2
HadGEM3-GC31-LL	r1i1p1f3	r1i1p1f1	r1i1p1f3
HadGEM3-GC31-MM	r1i1p1f3	r1i1p1f1	r1i1p1f3
INM-CM4-8	r1i1p1f1	r1i1p1f1	r1i1p1f1
INM-CM5-0	r1i1p1f1	r1i1p1f1	r1i1p1f1
IPSL-CM6A-LR	r1i1p1f1	r1i1p1f1	r1i1p1f1
KACE-1-0-G	r1i1p1f1	r1i1p1f1	r1i1p1f1
MIROC6	r1i1p1f1	r1i1p1f1	r1i1p1f1
MIROC-ES2L	r1i1p1f2	r1i1p1f2	r1i1p1f2
MPI-ESM1-2-HAM	r1i1p1f1	r1i1p1f1	
MPI-ESM1-2-HR	r1i1p1f1	r1i1p1f1	r1i1p1f1
MPI-ESM1-2-LR	r1i1p1f1	r1i1p1f1	r1i1p1f1
MRI-ESM2-0	r1i1p1f1	r1i1p1f1	r1i1p1f1
NorCPM1	r1i1p1f1	r1i1p1f1	
NorESM2-LM	r1i1p1f1	r1i1p1f1	r1i1p1f1
SAM0-UNICON	r1i1p1f1	r1i1p1f1	
TaiESM1	r1i1p1f1	r1i1p1f1	r1i1p1f1
UKESM1-0-LL	r1i1p1f2	r1i1p1f2	r1i1p1f2
UKESM1-1-LL	r1i1p1f2	r1i1p1f2	

Appendix A: CMIP6 simulation data used

Table A1 summarises the CMIP6 models, simulations and variants used in this study. For the *historical* and *piControl* simulations, data from 40 models were used. For the *SSP5-8.5* simulation, data from 35 models were used. For the *historical* simulations, a 35-year period spanning 1980 to 2014 is used to construct a climatology. For *SSP5-8.5*, 35 years of end-of-century data is used, spanning 2066–2100, for all models except CAMS-CSM1-0 and E3SM-1-0. For these models the year 2100 is not available, and the period used is instead 2065–2099. Given that the aim here is to diagnose broad patterns of energetic change across the century, and that models are expected to have different temperatures relative to preindustrial at end of century, this shift of a year for these two models is not expected to affect interpretation of the results.

For *piControl*, 400 years of data were used to create a climatology for each model, except for CNRM-CM6-1-HR, for which only 300 years was available. The 400 years selected are the final 400 years available for the simulation, except for CAMS-CSM1-0, for which 2900–3299 is used due to missing temperature data in the 3300–3324 file, and EC-Earth3-Veg and EC-Earth3-CC, for which 1950–2349 and 1955–2354 are used respectively, as not all variables span the full simulation length. These deviations are noted to support re-

producibility but are not expected to significantly influence results, given that piControl simulation is initiated after a spin-up period and a long period is used to form the climatologies.

Appendix B: Supplementary Figures

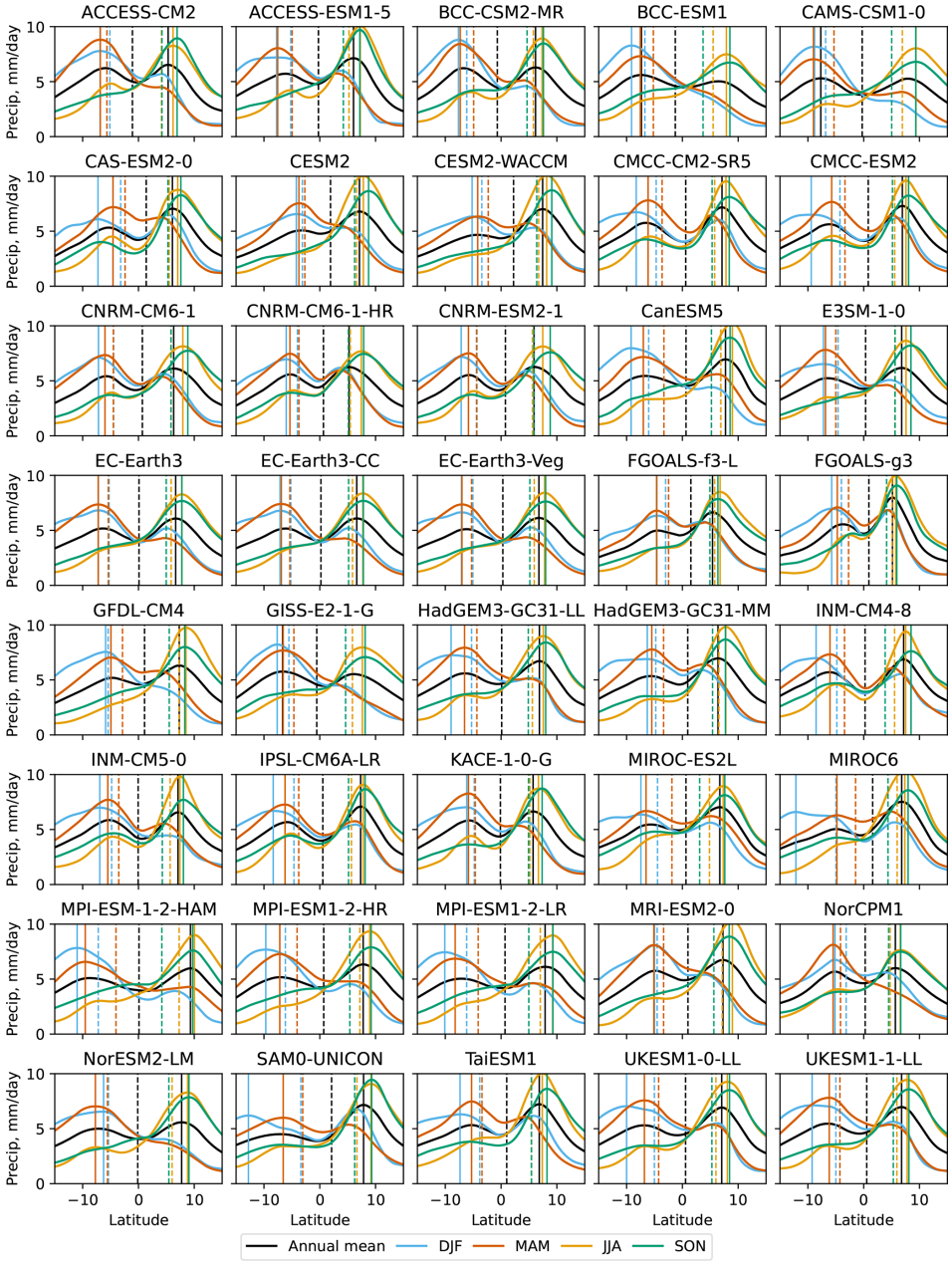

Figure B1. Zonal-mean precipitation for each model for each season and for the annual mean (black). Vertical lines show the precipitation centroid for each season (dashed) and the latitude of maximum precipitation (solid).

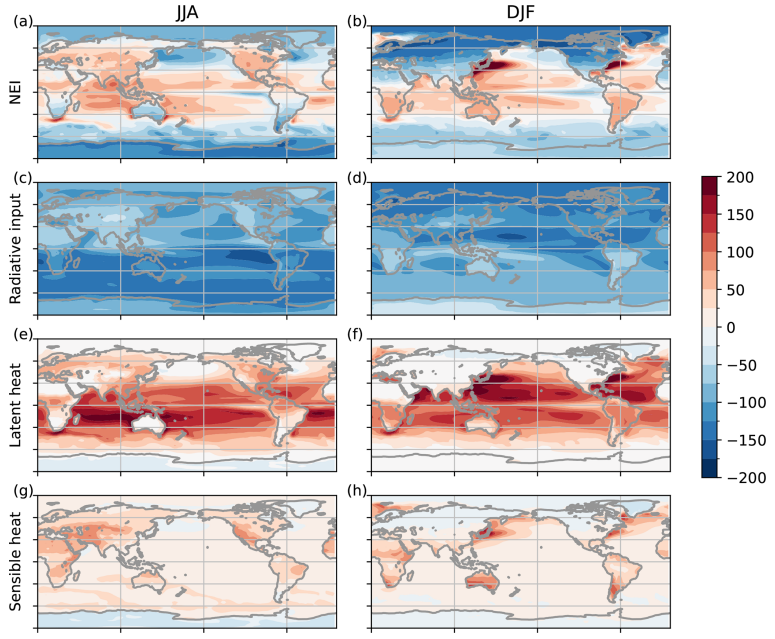

Figure B2. As Fig. 2 in the main text, but showing the corresponding energy fluxes (W m^{-2}, with sign convention so that positive is directed into the atmosphere.

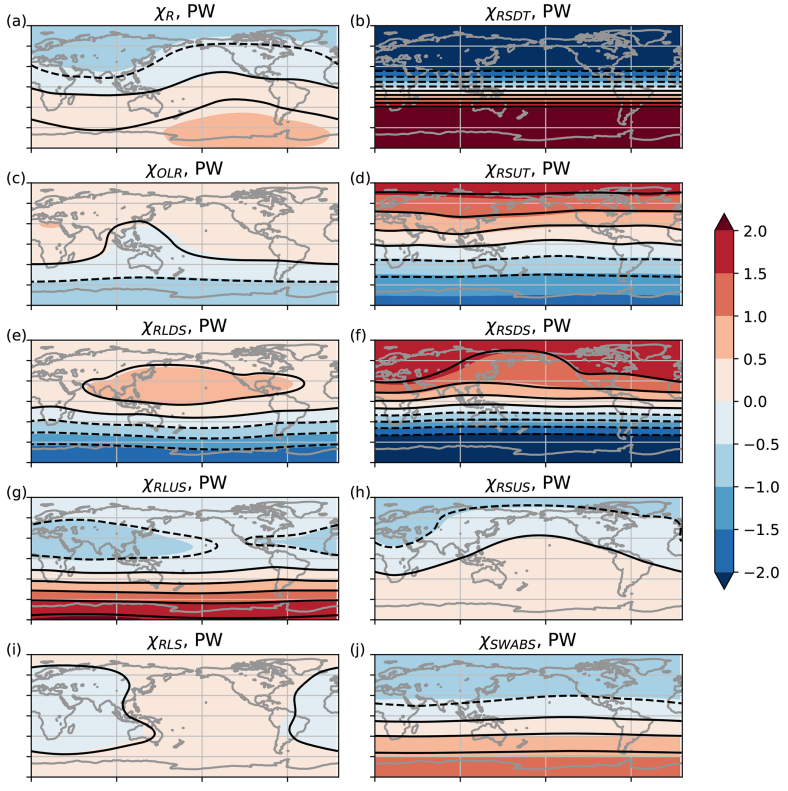

Figure B3. The figure shows the JJA breakdown of the radiative heating contribution to the energy flux potential, χ_R **(a)**, into χ_R components attributed to: **(b)** downward shortwave at the top of atmosphere, **(c)** outgoing longwave radiation, **(d)** upward shortwave at the top of atmosphere, downward surface **(e)** longwave and **(f)** shortwave, and upward surface **(g)** longwave and **(h)** shortwave. Panel **(i)** shows net surface longwave (sum of panels **e** and **g**). Panel **(j)** shows shortwave radiation absorbed in the atmosphere (sum of panels **b**, **d**, **f** and **h**).

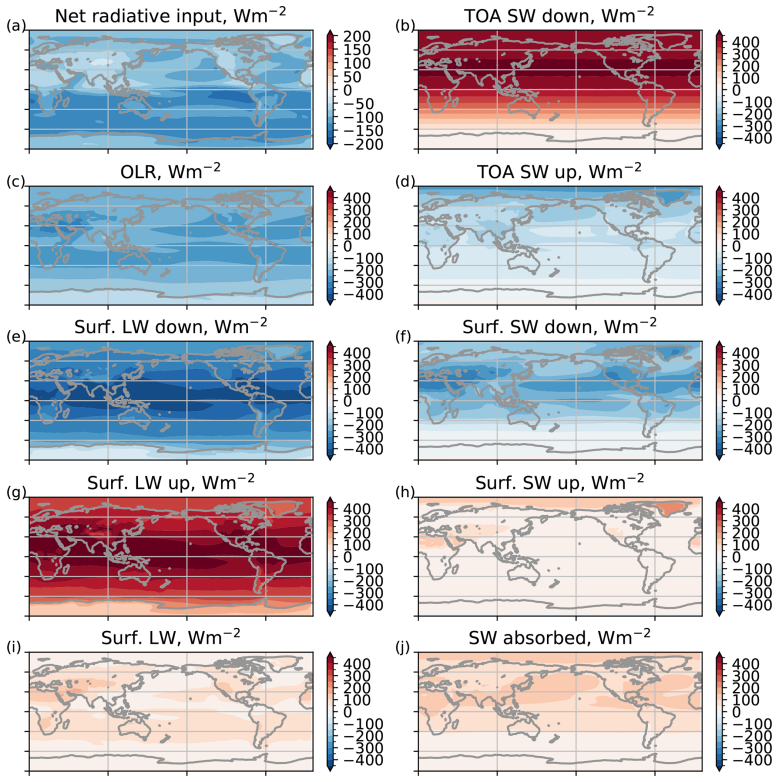

Figure B4. As Fig. B3 above but showing the corresponding energy fluxes, with sign convention so that positive is directed into the atmosphere.

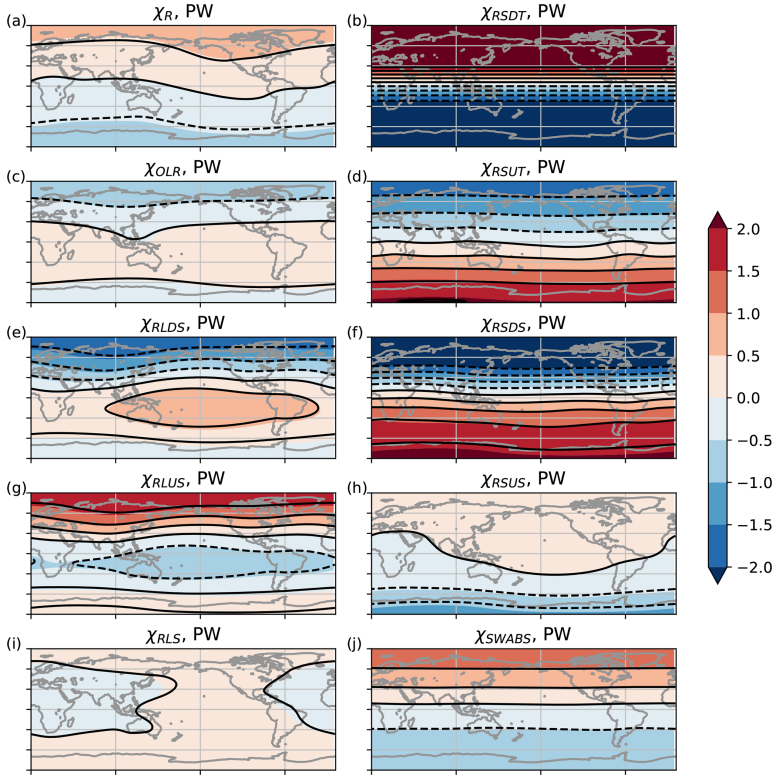

Figure B5. As Fig. B3 above, but for DJF.

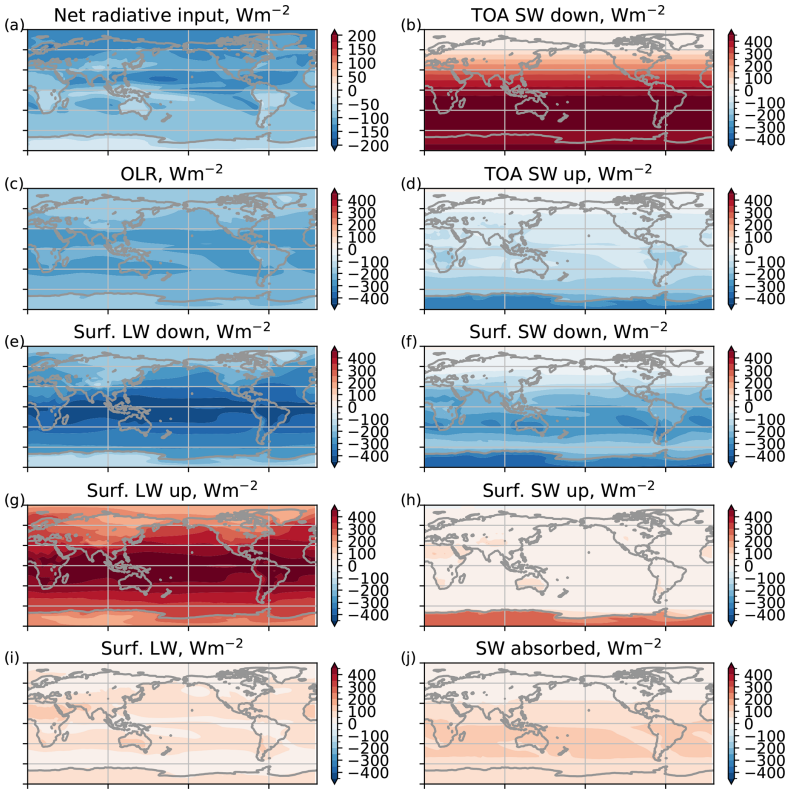

Figure B6. As Fig. B4 above, for DJF.

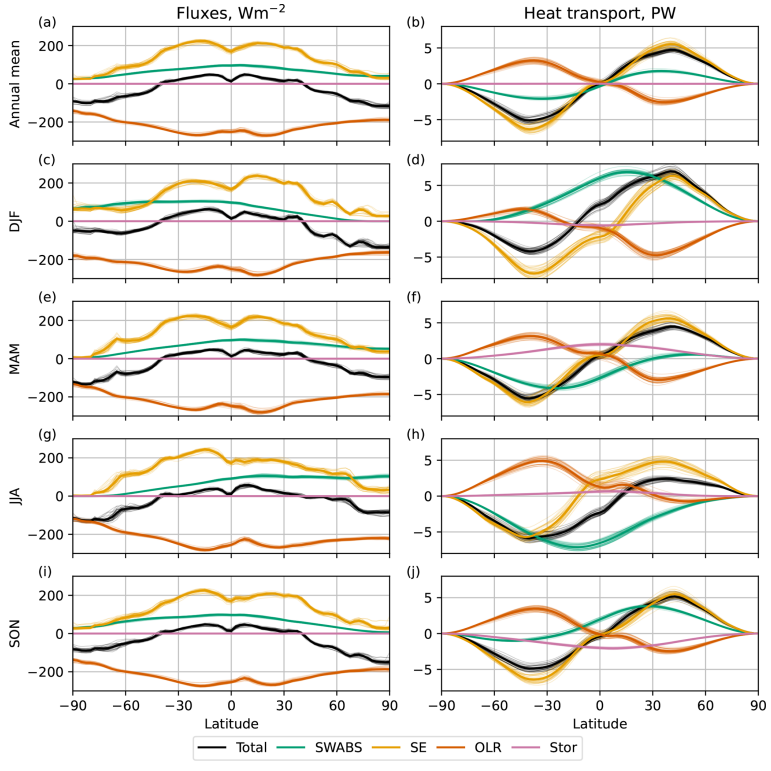

Figure B7. As Fig. 1 in the main text, but showing an alternative breakdown of the budget (cf. Donohoe et al., 2013; Kim et al., 2021).

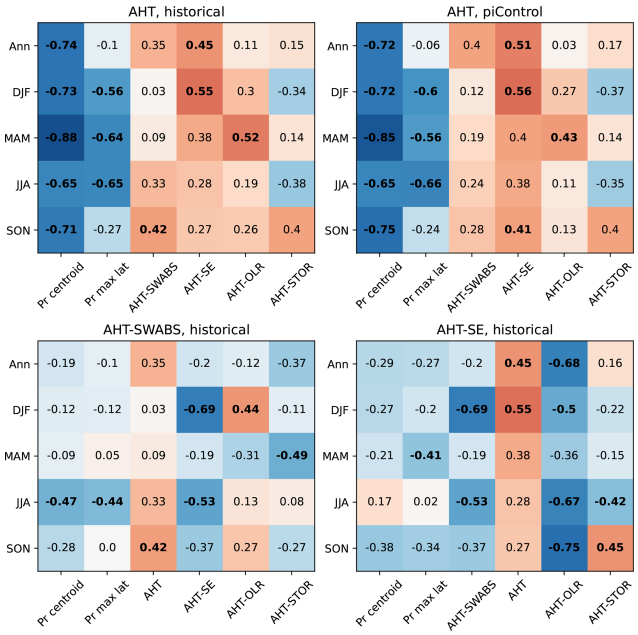

Figure B8. As Fig. 3 in the main text, but showing an alternative breakdown of the budget (cf. Donohoe et al., 2013; Kim et al., 2021).

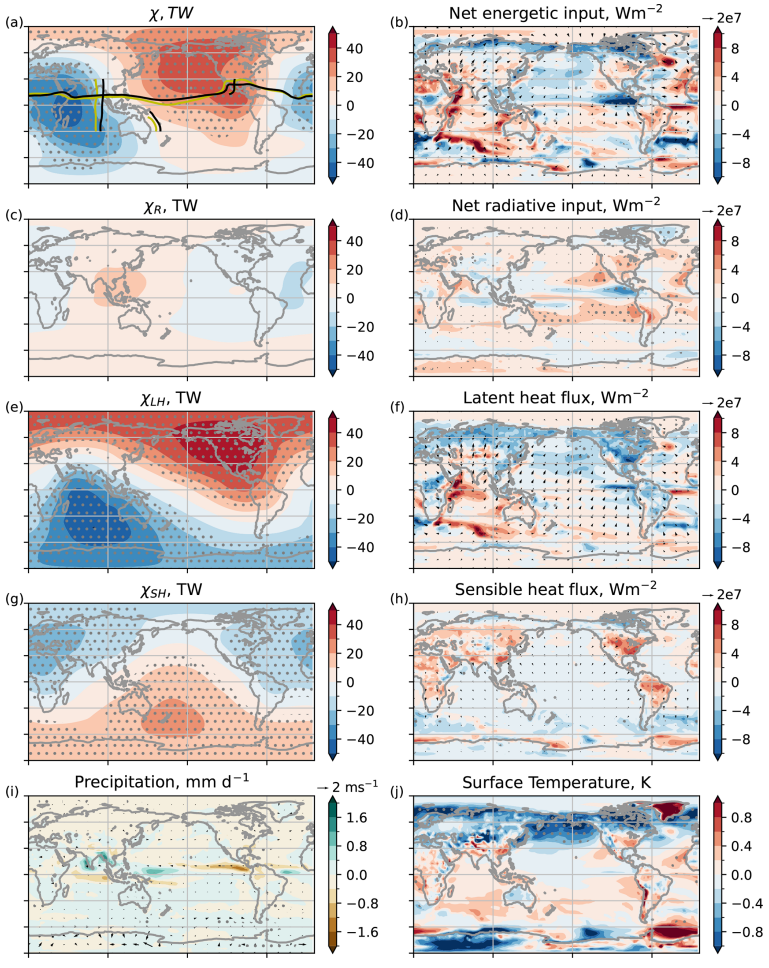

Figure B9. As Fig. 4 but for JJA PC3 (16.4 % of variance).

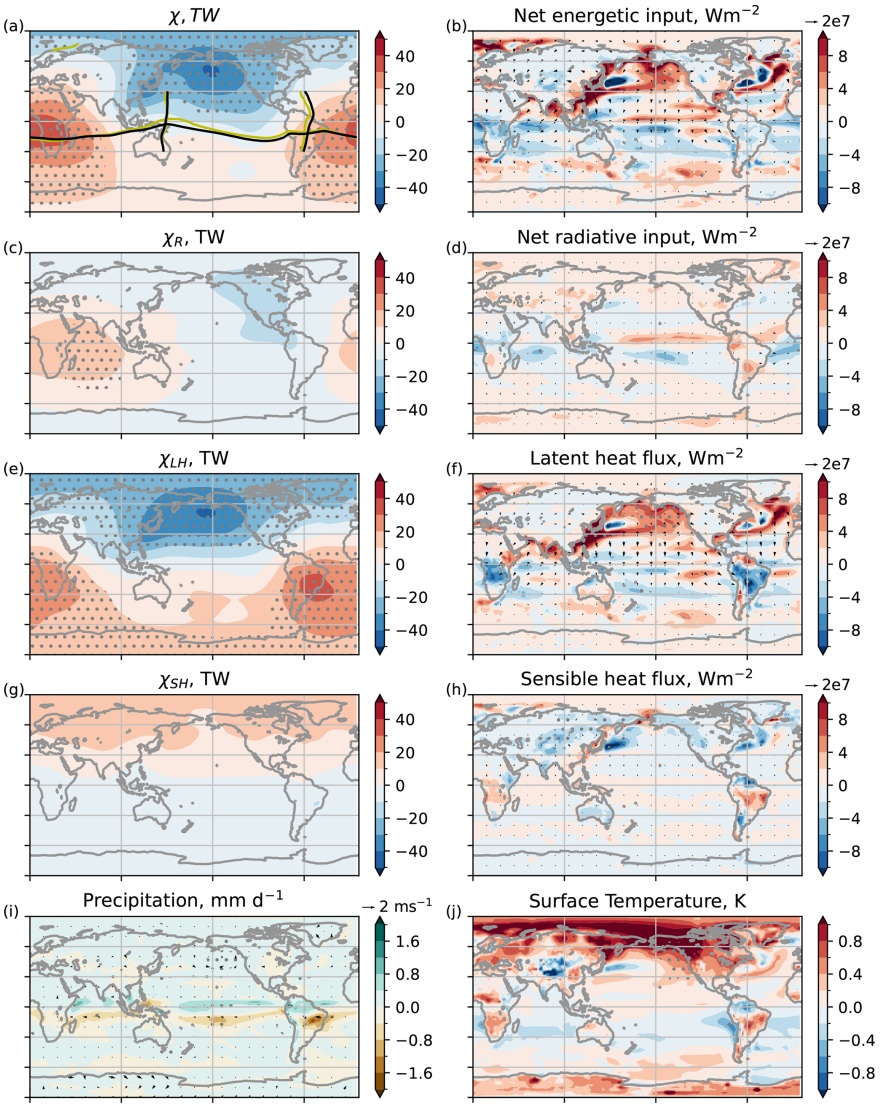

Figure B10. As Fig. 4 but for DJF PC3 (10.6 % of variance).

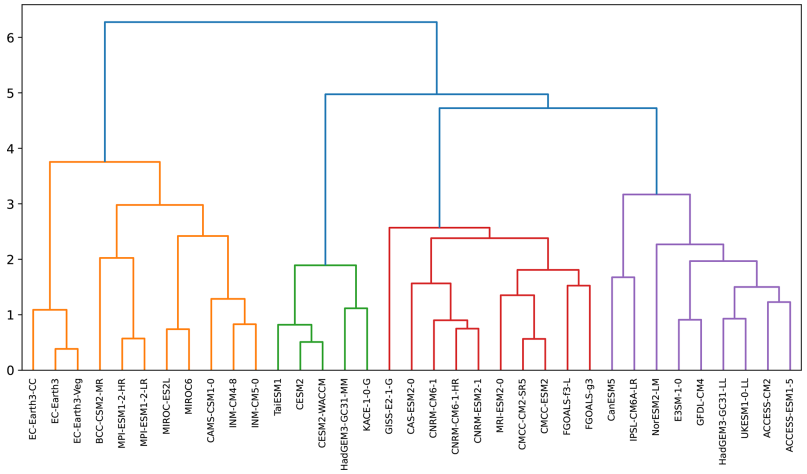

Figure B11. Dendrogram illustrating the result of hierarchical clustering applied to the differences between the *SSP5-8.5* and *historical* simulation for PCs 1–3 of χ, and the projections onto PCs 1–3 of the components of χ associated with radiative input, latent and sensible heat fluxes.

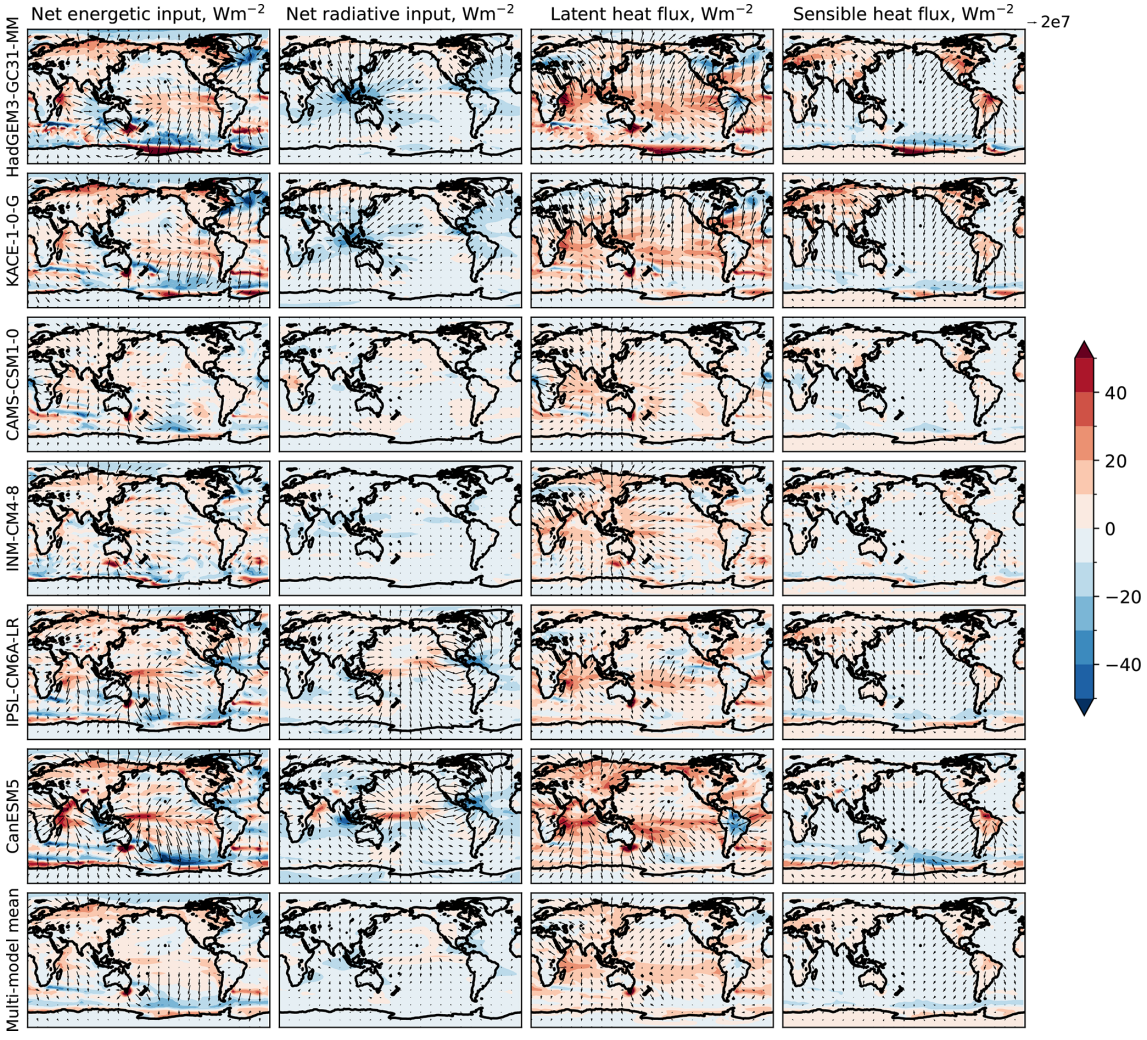

Figure B12. As Fig. 12 in the main text, but showing the corresponding energy fluxes.

Data availability. The CMIP6 data supporting the findings of this study are available via the Earth System Grid Federation (ESGF) nodes (https://esgf.github.io/nodes.html, last access: 13 December 2024). The ERA5 reanalysis is available from the Copernicus Climate Data Store (https://cds.climate.copernicus.eu/datasets/, last access: 5 July 2024).

Author contributions. R.G. designed the work, performed most of the analysis and drafted the manuscript. R.F. and M.L. supported interpretation of the data. I.M. performed the initial analysis motivating the paper and leading to Fig. 3.

Competing interests. The contact author has declared that none of the authors has any competing interests.

Disclaimer. Publisher's note: Copernicus Publications remains neutral with regard to jurisdictional claims made in the text, published maps, institutional affiliations, or any other geographical representation in this paper. The authors bear the ultimate responsibility for providing appropriate place names. Views expressed in the text are those of the authors and do not necessarily reflect the views of the publisher.

Financial support. RG was supported by the Natural Environment Research Council (grant number NE/X014827/1). RF was partially supported by a Natural Sciences and Engineering Research Council Discovery grant (award number RGPIN-2024-05745). ML was partially supported by the Natural Sciences and Engineering Research Council of Canada (award number RGPIN-2025-04261).

Review statement. This paper was edited by Yen-Ting Hwang and reviewed by two anonymous referees.

References

Adam, O., Bischoff, T., and Schneider, T.: Seasonal and interannual variations of the energy flux equator and ITCZ. Part I: Zonally averaged ITCZ position, J. Climate, 29, 3219–3230, https://doi.org/10.1175/JCLI-D-15-0512.1, 2016a.

Adam, O., Bischoff, T., and Schneider, T.: Seasonal and interannual variations of the energy flux equator and ITCZ. Part II: Zonally varying shifts of the ITCZ, J. Climate, 29, 7281–7293, https://doi.org/10.1175/JCLI-D-15-0710.1, 2016b.

Adam, O., Schneider, T., Brient, F., and Bischoff, T.: Relation of the double-ITCZ bias to the atmospheric energy budget in climate models, Geophys. Res. Lett., 43, 7670–7677, https://doi.org/10.1002/2016GL069465, 2016c.

Adam, O., Schneider, T., and Brient, F.: Regional and seasonal variations of the double-ITCZ bias in CMIP5 models, Clim. Dynam., 51, 101–117, https://doi.org/10.1007/s00382-017-3909-1, 2018.

Biasutti, M., Voigt, A., Boos, W. R., Braconnot, P., Hargreaves, J. C., Harrison, S. P., Kang, S. M., Mapes, B. E., Scheff, J., Schumacher, C., Sobel, A. H., and Xie, S.-P.: Global energetics and local physics as drivers of past, present and future monsoons, Nat. Geosci., 11, 392–400, https://doi.org/10.1038/s41561-018-0137-1, 2018.

Boos, W. R. and Korty, R. L.: Regional energy budget control of the intertropical convergence zone and application to mid-Holocene rainfall, Nat. Geosci., 9, 892–897, https://doi.org/10.1038/ngeo2833, 2016.

Chadwick, R., Boutle, I., and Martin, G.: Spatial patterns of precipitation change in CMIP5: Why the rich do not get richer in the tropics, J. Climate, 26, 3803–3822, 2013.

Chen, Z., Zhou, T., Chen, X., Zhang, W., Zhang, L., Wu, M., and Zou, L.: Observationally constrained projection of Afro-Asian monsoon precipitation, Nat. Commun., 13, 2552, https://doi.org/10.1038/s41467-022-30106-z, 2022.

Chen, Z., Zhou, T., Chen, X., Zhang, L., Qian, Y., Wang, Z., He, L., and Leung, L. R.: Understanding the biases in global monsoon simulations from the perspective of atmospheric energy transport, J. Climate, https://doi.org/10.1175/JCLI-D-23-0444.1, 2024.

Collins, M., An, S.-I., Cai, W., Ganachaud, A., Guilyardi, E., Jin, F.-F., Jochum, M., Lengaigne, M., Power, S., Timmermann, A., Vecchi, G., and Wittenberg, A.: The impact of global warming on the tropical Pacific Ocean and El Niño, Nat. Geosci., 3, 391–397, https://doi.org/10.1038/ngeo868, 2010.

Dawson, A.: eofs: A library for EOF analysis of meteorological, oceanographic, and climate data, Journal of Open Research Software, 4, https://doi.org/10.5334/jors.122, 2016.

Donohoe, A., Marshall, J., Ferreira, D., and Mcgee, D.: The relationship between ITCZ location and cross-equatorial atmospheric heat transport: From the seasonal cycle to the Last Glacial Maximum, J. Climate, 26, 3597–3618, https://doi.org/10.1175/JCLI-D-12-00467.1, 2013.

Donohoe, A., Atwood, A. R., and Byrne, M. P.: Controls on the width of tropical precipitation and its contraction under global warming, Geophys. Res. Lett., 46, 9958–9967, 2019.

Donohoe, A., Armour, K. C., Roe, G. H., Battisti, D. S., and Hahn, L.: The partitioning of meridional heat transport from the last glacial maximum to CO_2 quadrupling in coupled climate models, J. Climate, 33, 4141–4165, https://doi.org/10.1175/JCLI-D-19-0797.1, 2020.

Donohoe, A., Fajber, R., Cox, T., Armour, K., Battisti, D., and Roe, G.: Model biases in the atmosphere-ocean partitioning of poleward heat transport are persistent across three CMIP generations, Geophys. Res. Lett., 51, e2023GL106639, https://doi.org/10.1029/2023GL106639, 2024.

Eyring, V., Bony, S., Meehl, G. A., Senior, C. A., Stevens, B., Stouffer, R. J., and Taylor, K. E.: Overview of the Coupled Model Intercomparison Project Phase 6 (CMIP6) experimental design and organization, Geosci. Model Dev., 9, 1937–1958, https://doi.org/10.5194/gmd-9-1937-2016, 2016.

Fajber, R., Donohoe, A., Ragen, S., Armour, K. C., and Kushner, P. J.: Atmospheric heat transport is governed by meridional gradients in surface evaporation in modern-day earth-like climates, P. Natl. Acad. Sci. USA, 120, e2217202120, https://doi.org/10.1073/pnas.2217202120, 2023.

Frierson, D. M. and Hwang, Y.-T.: Extratropical influence on ITCZ shifts in slab ocean simulations of global warming, J. Climate, 25, 720–733, 2012.

Han, J., Nie, J., Hu, Y., Boos, W. R., Liu, Y., Yang, J., Yuan, S., Li, X., Guo, J., Lan, J., Lin, Q., Bao, X., Wei, M., Li, Z., Man, K., and Yin, Z.: Continental drift shifts tropical rainfall by altering radiation and ocean heat transport, Sci. Adv., 9, eadf7209, https://doi.org/10.1126/sciadv.adf7209, 2023.

Hersbach, H., Bell, B., Berrisford, P., Biavati, G., Horányi, A., Muñoz Sabater, J., Nicolas, J., Peubey, C., Radu, R., Rozum, I., Schepers, D., Simmons, A., Soci, C., Dee, D., and Thépaut, J.-N.: ERA5 monthly averaged data on single levels from 1940 to present, Copernicus Climate Change Service (C3S) Climate Data Store (CDS) [data set], https://doi.org/10.24381/cds.f17050d7, 2023.

Hyder, P., Edwards, J. M., Allan, R. P., Hewitt, H. T., Bracegirdle, T. J., Gregory, J. M., Wood, R. A., Meijers, A. J., Mulcahy, J., Field, P., Furtado, K., Bodas-Salcedo, A., Williams, K. D., Copsey, D., Josey, S. A., Liu, C., Roberts, C. D., Sanchez, C., Ridley, J., Thorpe, L., Hardiman, S. C., Mayer, M., Berry, D. I., and Belcher, S. E.: Critical Southern Ocean climate model biases traced to atmospheric model cloud errors, Nat. Commun., 9, 3625, https://doi.org/10.1038/s41467-018-05634-2, 2018.

Kang, S. M.: Extratropical influence on the tropical rainfall distribution, Current Climate Change Reports, 6, 24–36, https://doi.org/10.1007/s40641-020-00154-y, 2020.

Kang, S. M., Held, I. M., Frierson, D. M., and Zhao, M.: The response of the ITCZ to extratropical thermal forcing: Idealized slab-ocean experiments with a GCM, J. Climate, 21, 3521–3532, https://doi.org/10.1175/2007JCLI2146.1, 2008.

Kim, H., Kang, S. M., Takahashi, K., Donohoe, A., and Pendergrass, A. G.: Mechanisms of tropical precipitation biases in climate models, Clim. Dynam., 56, 17–27, https://doi.org/10.1007/s00382-020-05325-z, 2021.

Luo, F., Ying, J., Liu, T., and Chen, D.: Origins of Southern Ocean warm sea surface temperature bias in CMIP6 models, npj Clim. Atmos. Sci., 6, 127, https://doi.org/10.1038/s41612-023-00456-6, 2023.

Mamalakis, A., Randerson, J. T., Yu, J.-Y., Pritchard, M. S., Magnusdottir, G., Smyth, P., Levine, P. A., Yu, S., and Foufoula-Georgiou, E.: Zonally contrasting shifts of the tropical rain belt in response to climate change, Nat. Clim. Change, 11, 143–151, https://doi.org/10.1038/s41558-020-00963-x, 2021.

Mayer, J., Mayer, M., and Haimberger, L.: Consistency and homogeneity of atmospheric energy, moisture, and mass budgets in ERA5, J. Climate, 34, 3955–3974, https://doi.org/10.1175/JCLI-D-20-0676.1, 2021a.

Mayer, J., Mayer, M., and Haimberger, L.: Mass-consistent atmospheric energy and moisture budget monthly data from 1979 to present derived from ERA5 reanalysis, Copernicus Climate Change Service (C3S) Climate Data Store (CDS) [data set], https://doi.org/10.24381/cds.c2451f6b, 2021b.

Nicknish, P. A., Chiang, J. C., Hu, A., and Boos, W. R.: Regional tropical rainfall shifts under global warming: an energetic perspective, Environ. Res.: Climate, 2, 015007, https://doi.org/10.1088/2752-5295/acb9b0, 2023.

O'Neill, B. C., Tebaldi, C., van Vuuren, D. P., Eyring, V., Friedlingstein, P., Hurtt, G., Knutti, R., Kriegler, E., Lamarque, J.-F., Lowe, J., Meehl, G. A., Moss, R., Riahi, K., and Sanderson, B. M.: The Scenario Model Intercomparison Project (ScenarioMIP) for CMIP6, Geosci. Model Dev., 9, 3461–3482, https://doi.org/10.5194/gmd-9-3461-2016, 2016.

Ren, Z. and Zhou, T.: Understanding the alleviation of "Double-ITCZ" bias in CMIP6 models from the perspective of atmospheric energy balance, Clim. Dynam., 1–21, https://doi.org/10.1007/s00382-024-07238-7, 2024.

Schneider, T., Bischoff, T., and Haug, G. H.: Migrations and dynamics of the intertropical convergence zone, Nature, 513, 45–53, https://doi.org/10.1038/nature13636, 2014.

Stone, P. H.: Constraints on dynamical transports of energy on a spherical planet, Dynam. Atmos. Oceans, 2, 123–139, https://doi.org/10.1016/0377-0265(78)90006-4, 1978.

Trenberth, K. E. and Stepaniak, D. P.: Seamless poleward atmospheric energy transports and implications for the Hadley circulation, J. Climate, 16, 3706–3722, https://doi.org/10.1175/1520-0442(2003)016<3706:SPAETA>2.0.CO;2, 2003.

Trenberth, K. E. and Stepaniak, D. P.: The flow of energy through the Earth's climate system, Q. J. Roy. Meteor. Soc., 130, 2677–2701, https://doi.org/10.1256/qj.04.83, 2004.

Tuckman, P., Smyth, J., Lutsko, N. J., and Marshall, J.: The zonal seasonal cycle of tropical precipitation: Introducing the Indo-Pacific monsoonal mode, J. Climate, 37, 3807–3824, 2024.

Vallis, G. K., Colyer, G., Geen, R., Gerber, E., Jucker, M., Maher, P., Paterson, A., Pietschnig, M., Penn, J., and Thomson, S. I.: Isca, v1.0: a framework for the global modelling of the atmospheres of Earth and other planets at varying levels of complexity, Geosci. Model Dev., 11, 843–859, https://doi.org/10.5194/gmd-11-843-2018, 2018.

Wang, C., Zhang, L., Lee, S.-K., Wu, L., and Mechoso, C. R.: A global perspective on CMIP5 climate model biases, Nat. Clim. Change, 4, 201–205, https://doi.org/10.1038/nclimate2118, 2014.

Wilks, D.: "The stippling shows statistically significant grid points": How research results are routinely overstated and overinterpreted, and what to do about it, B. Am. Meteorol. Soc., 97, 2263–2273, https://doi.org/10.1175/BAMS-D-15-00267.1, 2016.

Yang, H., Li, Q., Wang, K., Sun, Y., and Sun, D.: Decomposing the meridional heat transport in the climate system, Clim. Dynam., 44, 2751–2768, https://doi.org/10.1007/s00382-014-2380-5, 2015.